

# Electronic Band Structure of Moiré Systems from Microscopic Tight Binding Models

Bachelor-Arbeit  
zur Erlangung des Hochschulgrades  
Bachelor of Science  
im Bachelor-Studiengang Physik

vorgelegt von

Jan Biedermann  
geboren am 10.06.2002 in Bischofswerda

Institut für Theoretische Physik  
Fakultät Physik  
Bereich Mathematik und Naturwissenschaften  
Technische Universität Dresden  
2024

Eingereicht am 23. Mai 2024

1. Gutachter: Dr. Lukas Janssen
2. Gutachter: Prof. Dr. Matthias Vojta

---

## Abstract

Owing to the discovery of correlated insulating and superconducting phases in twisted graphene bilayers, moiré materials have garnered an immense amount of interest in the field of strongly correlated materials research. In this thesis, we study the electronic band structure of twisted bilayer graphene (TBG) with an existing tight binding model and compare the results to those obtained from the effective Bistritzer-MacDonald continuum Hamiltonian. This includes an investigation of Van Hove singularities in the dispersion, as well as the effective *Fermi* velocity of electrons at the linearly dispersive Dirac points. We additionally model the effect of Coulomb interactions between electrons by means of a generalized Hubbard Hamiltonian in the mean-field approximation. Two candidate ground states reported in the literature are parametrized for the Hubbard Hamiltonian, and the evolution of their order parameters as a function of the twist angle is illustrated in several quantum phase diagrams. Our results complement a series of recent Hartree-Fock studies on insulating ground states in TBG based on the Bistritzer-MacDonald Hamiltonian.

## Kurzzusammenfassung

Seit der Entdeckung korrelierter isolierender und supraleitender Grundzustände in Twisted Bilayer Graphene (TBG) sind Moiré-Heterostrukturen von großem Interesse für die Erforschung stark korrelierter Elektronen. In dieser Arbeit untersuchen wir die elektronische Bandstruktur von TBG mit einem existierenden Tight-Binding Hamiltonian und vergleichen die Ergebnisse mit denen des effektiven Bistritzer-MacDonald Kontinuums-Hamiltonian. Dabei werden auch Van Hove-Singularitäten in der Dispersion, sowie die effektive *Fermi* Geschwindigkeit von Elektronen an den linear dispersiven Dirac-Punkten betrachtet. Wir modellieren zusätzlich die Auswirkungen der Coulomb Wechselwirkung zwischen Elektronen mittels eines verallgemeinerten Hubbard Hamiltonians im Rahmen der Molekularfeldtheorie. Zwei potenzielle Grundzustände aus der Literatur werden für den Hubbard Hamiltonian parametrisiert, und die Entwicklung ihrer Ordnungsparameter als Funktion des Twist-Winkels wird in mehreren Quantenphasendiagrammen dargestellt. Unsere Ergebnisse ergänzen eine Reihe von Hartree-Fock Studien zu den isolierenden Grundzuständen von TBG auf Grundlage des Bistritzer-MacDonald Hamiltonians.



# Contents

<b>1</b>	<b>Introduction</b>	<b>1</b>
<b>2</b>	<b>Single-particle physics</b>	<b>3</b>
2.1	Preliminaries . . . . .	3
2.2	Geometry of twisted graphene bilayers . . . . .	7
2.3	Microscopic tight binding model . . . . .	10
2.4	Continuum model . . . . .	12
2.5	Approximation of incommensurate twist angles . . . . .	16
2.6	Electronic band structure . . . . .	17
2.7	Density of states and Van Hove singularities . . . . .	20
2.8	Band separation and Fermi velocity . . . . .	23
<b>3</b>	<b>Interactions</b>	<b>29</b>
3.1	Mean-field approximation . . . . .	29
3.2	Electron-electron interactions in the microscopic model . . . . .	31
3.3	Current operator for the generalized Hubbard Hamiltonian . . . . .	34
3.4	Candidate ground states . . . . .	34
3.5	Quantum phase diagrams . . . . .	41
<b>4</b>	<b>Summary and Outlook</b>	<b>45</b>
<b>5</b>	<b>Bibliography</b>	<b>47</b>



# 1 Introduction

Due to what is essentially a happy accident, Coulomb interactions between conduction electrons in traditional solids can usually be neglected entirely when studying their electronic properties. This is a central result of the framework of Fermi liquid theory, where low-energy conduction electrons are shown to behave essentially like free electrons, though with a renormalized mass [1]. However, non-Fermi liquid behaviour has since been observed in cuprate materials, inducing unconventional high-temperature superconductivity [1, 2], and paving the way for research on strongly correlated electrons. Novel correlated phases of matter are exciting physical discoveries in their own right, but superconducting solids in particular are also promising candidates for technological applications.

More recently, two-dimensional moiré materials have emerged as an alternative platform for the experimental realization of strongly correlated phases [3]: At the forefront of this novel class of materials is twisted bilayer graphene (TBG), where a relative twist is introduced between two stacked graphene sheets. At certain discrete twist angles, the two rotated graphene monolayers are aligned such that their atoms form a rigorously periodic crystal lattice, visually creating the impression of an intricate moiré pattern. A single unit cell of this moiré superlattice can contain thousands of individual carbon atoms, and this increase in the real-space lattice constant is associated with a contraction of the moiré Brillouin zone. Hence, TBG exhibits heavily folded electronic energy bands, and the typical band widths of the system are much smaller than those in monolayer graphene, magnifying the relative energy scale of Coulomb interactions. Modern experimental tools even allow for an adjustment of the twist angle in a single sample, thus promoting the ratio of kinetic energy and interaction strength to an experimentally tunable quantity [4]. The two-dimensional geometry also facilitates additional experimental manipulations, for instance allowing for electrostatic doping by means of an electrical gate, as opposed to the usual chemical doping in bulk materials [2, 3]. Of particular interest to the correlated physics of TBG are a series of *magic* twist angles where the bands closest to the Fermi energy are only weakly dispersive, causing Van Hove singularities in neighbouring bands to merge, further stimulating the occurrence of electron-electron interactions [3, 5]. A number of similar moiré heterostructures have also been investigated, including twisted graphene multilayers consisting of more than two graphene sheets [3].

This thesis is concerned with the properties of both the non-interacting energy bands of TBG, and the effects of Coulomb interactions in the material. The former are studied in Chapter 2

by means of the tight binding approximation, as well as an effective continuum model for the moiré superlattice [5]. To introduce electron-electron interactions into this description, we apply a mean-field decoupling to a generalized Hubbard Hamiltonian for TBG. Two correlated candidate ground states for this Hamiltonian are investigated in Chapter 3. Our Hubbard model analysis complements a number of Hartree-Fock studies on the correlated insulating ground states that are based on the continuum Hamiltonian for TBG [6–8]. We specifically focus on the impact of an effective twist angle on the presence of correlated phases. Finally, Chapter 4 summarizes our results and briefly discusses possible extensions.



# 2 Single-particle physics

## 2.1 Preliminaries

When carbon atoms are arranged in a honeycomb lattice, they form a two-dimensional sheet of graphene, first successfully isolated by A. K. Geim and K. S. Novoselov in 2004, earning them the 2010 Nobel prize in physics. Among the many exotic electronic properties of graphene, perhaps the most unusual is the presence of a pair of linearly dispersing Dirac cones in its electronic spectrum, where the effective behaviour of electrons resembles that of massless Dirac fermions, but with a velocity 300 times smaller than the speed of light [9].

As indicated in Fig. 2.1, each unit cell of the graphene lattice contains two lattice sites, forming an A and B sublattice, respectively. The displacement between neighbouring A and B sites is given by the nearest neighbour vectors

$$\boldsymbol{\delta}_1 = \frac{a_0}{2} \left( \sqrt{3}\mathbf{e}_x + \mathbf{e}_y \right), \quad (2.1)$$

$$\boldsymbol{\delta}_2 = \frac{a_0}{2} \left( -\sqrt{3}\mathbf{e}_x + \mathbf{e}_y \right), \quad (2.2)$$

$$\boldsymbol{\delta}_3 = -a_0\mathbf{e}_y, \quad (2.3)$$

and adjacent unit cells are related by the graphene lattice vectors

$$\mathbf{a}_1 = a\mathbf{e}_x, \quad (2.4)$$

$$\mathbf{a}_2 = \frac{a}{2} \left( \mathbf{e}_x + \sqrt{3}\mathbf{e}_y \right), \quad (2.5)$$

where  $a_0 \approx 0.142$  nm is the nearest neighbour distance and  $a = \sqrt{3}a_0$  is the lattice constant [2]. The corresponding reciprocal lattice is itself a honeycomb lattice with lattice vectors

$$\mathbf{b}_1 = \frac{2\pi}{\sqrt{3}a} \left( \mathbf{e}_x - \frac{1}{\sqrt{3}}\mathbf{e}_y \right), \quad (2.6)$$

$$\mathbf{b}_2 = \frac{4\pi}{3a}\mathbf{e}_y. \quad (2.7)$$

The basic electronic properties of graphene are readily determined with the help of the tight binding approximation. The idea is to construct solutions to the problem of electrons moving in a periodic potential from linear combinations of atomic orbitals. Although the tight binding

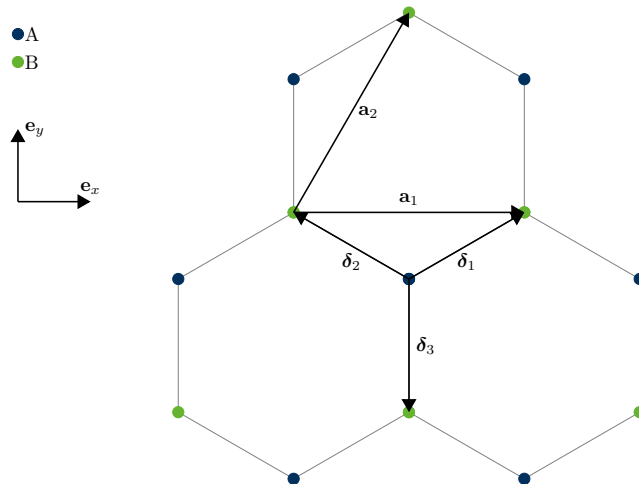


**Figure 2.1:** Graphene lattice consisting of an A and B sublattice with nearest neighbour vectors  $\delta_i$  and lattice vectors  $\mathbf{a}_j$ .

approximation yields an effective single particle description, it is conveniently expressed in the language of second quantization: For simplicity, suppose that each atom in the lattice contributes only a single delocalized electron and there is only one available orbital per lattice site. The first-quantized Hamiltonian will have the form [2]

$$\begin{aligned} H &= \sum_{j,\sigma} H_{j\sigma} \\ &= \sum_{j,\sigma} \left( T_j + \sum_i V(\mathbf{r}_j - \mathbf{R}_i) \right), \end{aligned}$$

where  $T_j$  is the operator of kinetic energy for electron  $j$ , and  $V(\mathbf{r} - \mathbf{R})$  is an effective potential generated by a nucleus (and possible localized electrons) at position  $\mathbf{R}$ . The summation  $\sum_i$  over the lattice sites  $\mathbf{R}_i$  aggregates the potentials of the individual nuclei, and  $\sum_{j,\sigma}$  ranges over all electrons in the lattice.

Since  $H$  is a sum of single particle observables, the corresponding second-quantized Hamiltonian will have the form [10]

$$\mathcal{H} = \sum_{\nu,\nu'} \langle \nu | H^{(1)} | \nu' \rangle c_{\nu}^{\dagger} c_{\nu'},$$

with  $H^{(1)} = T + \sum_i V(\mathbf{r} - \mathbf{R}_i)$  and  $|\nu\rangle$  a suitable basis of the single particle Hilbert space. The key insight of the tight binding approximation [2, 11] is that, assuming the effective potential decays sufficiently quickly, the single particle Hamiltonian  $H_{j\sigma}$  can be understood as

a perturbed atomic Hamiltonian, i.e.

$$H_{j\sigma} = \underbrace{T_j + V(\mathbf{r}_j - \mathbf{R}_j)}_{=H_j^0} + \Delta V(\mathbf{r}_j),$$

with  $\Delta V(\mathbf{r}_j) = \sum_{i \neq j} V(\mathbf{r}_j - \mathbf{R}_i)$  small compared to  $V$  in the vicinity of the nucleus. Hence, an approximate single particle basis  $|\nu\rangle$  is given by the (non-orthogonal) atomic orbitals  $|j\sigma\rangle$  for each site  $j$  and spin species  $\sigma$ . We may then write

$$\mathcal{H} = \sum_{j,\sigma} \langle j\sigma | H^{(1)} | j\sigma \rangle c_{j\sigma}^\dagger c_{j\sigma} + \sum_{i \neq j, \sigma, \sigma'} t_{ij} \delta_{\sigma\sigma'} c_{i\sigma}^\dagger c_{j\sigma},$$

where the onsite energies  $\langle j\sigma | H^{(1)} | j\sigma \rangle$  only contribute a constant energy shift and can be dropped. If the atomic orbitals are well-localized, the hopping terms  $t_{ij} = \langle i | H^{(1)} | j \rangle$  will become negligibly small once the interatomic separation  $|\mathbf{R}_i - \mathbf{R}_j|$  exceeds a certain threshold. In the simplest case, only hoppings between nearest neighbour sites are taken into consideration.

Although each carbon atom in a graphene sheet contributes a total of six electrons to the lattice, two of these electrons are tightly bound to the nucleus in low energy 1s orbitals, and an additional three electrons are shared with neighbouring carbon atoms in  $\sigma$  bonds [2]. The remaining electron occupies a  $2p_z$  orbital oriented perpendicularly to the lattice, where it becomes delocalized over the graphene sheet due to tunneling between adjacent  $p_z$  orbitals [2]. The resulting bonds are known as  $\pi$  bonds, and neglecting hoppings beyond nearest neighbour atoms, a second-quantized Hamiltonian for the  $\pi$  electrons is given by [9]

$$\mathcal{H} = -t \sum_{\langle i,j \rangle, \sigma} \left( c_{j\sigma}^\dagger c_{i\sigma} + \text{h.c.} \right),$$

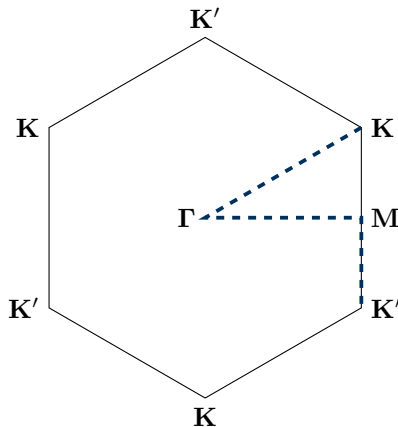


**Figure 2.2:** First Brillouin zone and high symmetry points of monolayer graphene and TBG. The dashed line represents the Brillouin zone path that we will focus on in the present text.

where  $c_{j\sigma}^\dagger$  creates an electron at site  $j$  with spin  $\sigma$ . Here,  $\sum_{\langle i,j \rangle}$  is taken over all nearest neighbour bonds in the lattice, and the nearest neighbour hopping amplitude is known to be  $t \approx 2.7 \text{ eV}$  [9]. Since  $t$  does not depend on spin, we may drop the sum over the spin degree of freedom when solving for the energy bands. Fourier transforming the Hamiltonian, one then readily obtains

$$\mathcal{H} = -t \sum_{\mathbf{k}} \underbrace{\Psi_{\mathbf{k}}^\dagger \begin{pmatrix} 0 & f(\mathbf{k}) \\ f(\mathbf{k})^* & 0 \end{pmatrix} \Psi_{\mathbf{k}}}_{=:h(\mathbf{k})},$$

where  $f(\mathbf{k}) = \sum_{j=1}^3 e^{i\mathbf{k}\cdot\delta_j}$ , and  $\Psi_{\mathbf{k}}^\dagger = (c_A^\dagger(\mathbf{k}), c_B^\dagger(\mathbf{k}))$  is a vector of creation operators for the A and B sublattice. The resulting eigenenergies are given by  $\varepsilon(\mathbf{k}) = \pm t|f(\mathbf{k})|$ . For the Brillouin zone path shown in Fig. 2.2, the band structure is plotted in Fig. 2.3.

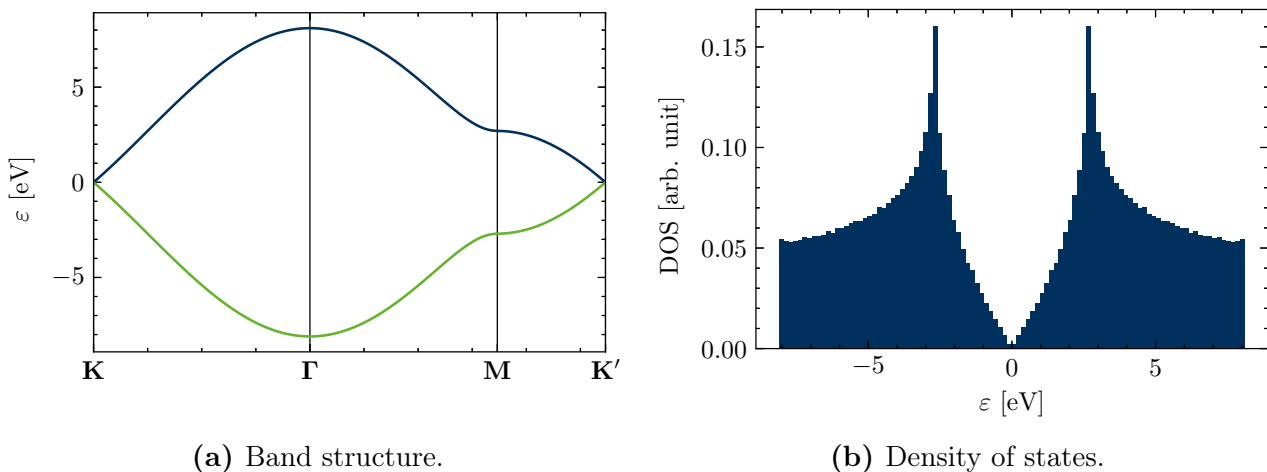


**Figure 2.3:** Tight binding band structure and density of states for monolayer graphene.

Additional insights can be gained from a low energy expansion of the dispersion around either of the band touching points

$$\mathbf{K}_- = \mathbf{K} = \frac{1}{3}(2\mathbf{b}_1 + \mathbf{b}_2), \quad (2.8)$$

$$\mathbf{K}_+ = \mathbf{K}' = \frac{1}{3}(\mathbf{b}_1 + 2\mathbf{b}_2), \quad (2.9)$$

where one finds  $\varepsilon(\mathbf{k}) \approx \pm v_F \hbar |\mathbf{k} - \mathbf{K}_\xi|$  for  $\mathbf{K}_\xi = \mathbf{K}, \mathbf{K}'$  [9]. Hence, instead of the familiar parabolic dispersion of non-relativistic free fermions, the behaviour of electrons resembles the conical dispersion of massless Dirac fermions. The effective velocity of  $v_F = 3a_0t/2\hbar \approx c/300$  is termed the Fermi velocity.

In the vicinity of the Fermi energy  $\varepsilon_F = 0$ , the corresponding density of states  $\rho$  can be shown to behave as  $\rho(\varepsilon) \sim |\varepsilon|$  [9]. Hence, there exists neither a Fermi surface nor a band gap in freestanding graphene, and in the absence of electron-electron interactions, the material can

thus be classified as a semimetal. Further away from the Fermi energy, Fig. 2.3b illustrates the presence of peaks in the density of states at energies  $\varepsilon = \pm t$ . These *Van Hove singularities* correspond to weakly dispersive patches in the spectrum at energies  $\pm t$ , where a large number of states can be accommodated. More precisely, it can be shown that the presence of Van Hove singularities in two-dimensional systems is associated with saddle points in the dispersion [11], which, in monolayer graphene, are located at the high symmetry  $\mathbf{M}$  points.

## 2.2 Geometry of twisted graphene bilayers

Modern experimental tools allow for the combination of two isolated sheets of graphene in a multitude of geometric configurations with different electronic properties. Perhaps the most simple such configuration is the AA stacking arrangement shown in Fig. 2.4a, where both the A and B sublattices of the individual layers are aligned with one another. In naturally occurring graphite, sheets of graphene are instead arranged in the energetically favourable AB stacking configuration [12] illustrated in Fig. 2.4b, where only the A sublattice of the top layer is aligned with the B sublattice of the bottom layer.

More generally, one can transform an AA stacked bilayer into a countably infinite number of periodic crystal lattices by twisting the bilayer by certain *commensurate* twist angles. Some examples of commensurate configurations are shown in Fig. 2.5. The twisted bilayer is most conveniently described in a coordinate system where the center of rotation is located at the origin, and for a total twist of  $\theta$ , the top (bottom) layer is rotated by an angle of  $-\theta/2$  ( $+\theta/2$ ). We will assume the axis of rotation passes through an A site in both layers, and denote the corresponding two-dimensional rotation matrices by  $\mathcal{R}(\mp\theta/2)$ .

We can find a general condition for commensurability of twist angles by introducing the notion of a *commensurate pair*, i.e. a pair of lattice sites, one in the top and one in the bottom layer, that are rotated precisely on top of one another. The moiré superlattice is commensurate if and only if it contains a commensurate pair, besides the commensurate pair at the origin where the layers necessarily coincide <sup>1</sup> [14]. This can be seen from the following argument:

- Periodic  $\Rightarrow$  commensurate pairs: Clearly, a lattice in which the origin is the only commensurate pair must violate translational symmetry, since no translation could map the origin into itself. Hence, the contrapositive of the claim holds.
- Commensurate pairs  $\Rightarrow$  periodic: Denote the primitive lattice vectors of the top (bottom) layer by  $\mathbf{a}_1^-$ ,  $\mathbf{a}_2^-$  ( $\mathbf{a}_1^+$ ,  $\mathbf{a}_2^+$ ) and assume there exists a commensurate pair  $\mathbf{L}_1 = m_- \mathbf{a}_1^- + n_- \mathbf{a}_2^- = m_+ \mathbf{a}_1^+ + n_+ \mathbf{a}_2^+$ . Since both layers are invariant under translations by  $\mathbf{L}_1$ , the moiré superlattice must also be invariant under such translations. Due to the threefold rotational symmetry of graphene, the lattice must additionally be invariant

---

<sup>1</sup>An equivalent commensurability condition with an alternative proof can be found in Ref. [13].

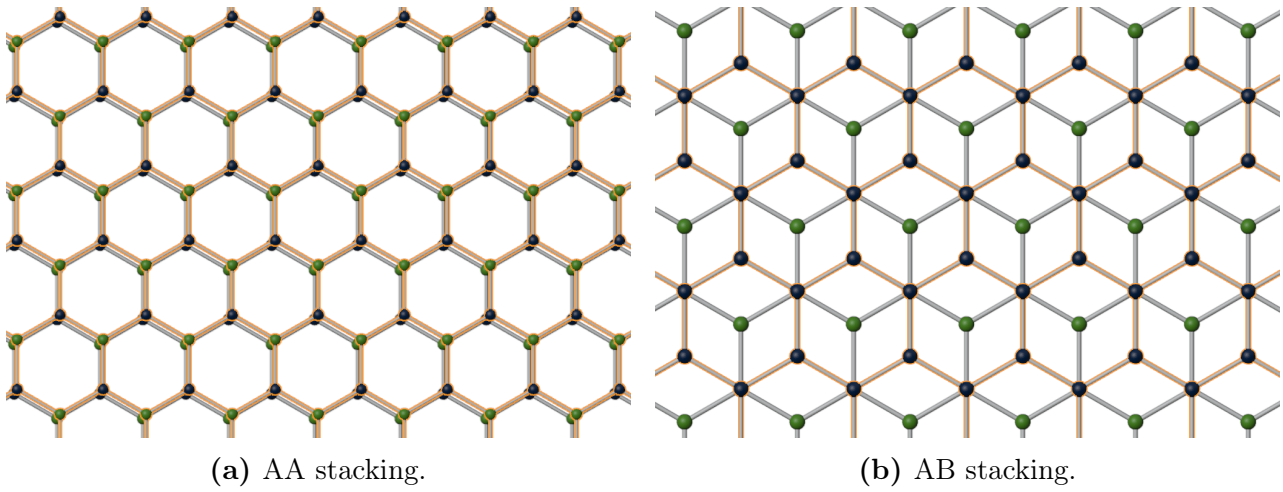


**Figure 2.4:** Elementary examples for periodic configurations of a graphene bilayer. The top layer is highlighted in orange, and the A and B sublattice are shown in blue and green, respectively.

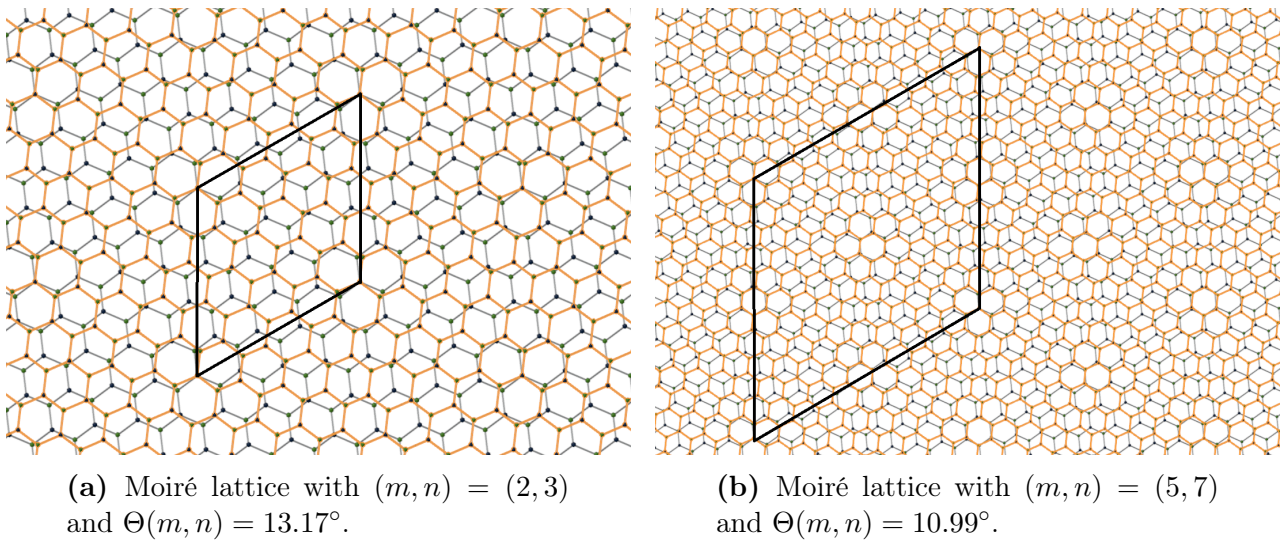


**Figure 2.5:** Moiré superlattices at different twist angles. The moiré unit cell is highlighted in bold. Note how locally, both lattices consist of regions of approximate AB, BA and AA stacking. In addition, the configuration with  $|m - n| = 2$  is approximately periodic with a period of  $1/|m - n|$  its actual lattice constant.

under translations by  $\mathcal{R}(-120^\circ)\mathbf{L}_1$ , and hence also  $\mathbf{L}_2 = -\mathcal{R}(-120^\circ)\mathbf{L}_1 = \mathcal{R}(60^\circ)\mathbf{L}_1$ . Note that the lattice vectors  $\mathbf{L}_1, \mathbf{L}_2$  given here are not necessarily primitive. We will discuss the primitive lattice vectors of TBG below.

Exploiting the relationship between commensurate twist angles and commensurate pairs, we can thus determine the set of commensurate twist angles by finding all lattice vectors  $\mathbf{R}_1, \mathbf{R}_2$  in the unrotated monolayer such that there exists some  $\theta$  with  $\mathcal{R}(-\theta/2)\mathbf{R}_1 = \mathcal{R}(\theta/2)\mathbf{R}_2$ . This is equivalent to finding all pairs of lattice vectors  $\mathbf{R}_1, \mathbf{R}_2$  located on a circle of radius  $|\mathbf{R}_1| = |\mathbf{R}_2|$ . In general, the problem of finding lattice points on a circle gives rise to a difficult Diophantine equation with a variable number of solutions. However, one can exploit the sixfold rotational symmetry of monolayer graphene to show that for  $0 \leq \theta \leq \pi/3$ , all commensurate twist angles can be determined from the solution  $\mathbf{R}_1 = m\mathbf{a}_1 + n\mathbf{a}_2$ ,  $\mathbf{R}_2 = n\mathbf{a}_1 + m\mathbf{a}_2$  with  $m, n \geq 0$  [14]. By some algebra, this yields the commensurate twist angles

$$\begin{aligned} \Theta(m, n) &= \arccos\left(\frac{\mathbf{R}_1 \cdot \mathbf{R}_2}{|\mathbf{R}_1||\mathbf{R}_2|}\right) \\ &= \arccos\left(\frac{1}{2} \frac{m^2 + n^2 + 4mn}{m^2 + n^2 + mn}\right). \end{aligned} \quad (2.10)$$

From the derivation above, it is evident that the lattice is invariant under translations by

$$\mathbf{L}_1 = m\mathbf{a}_1^- + n\mathbf{a}_2^-, \quad (2.11)$$

$$\mathbf{L}_2 = \mathcal{R}(60^\circ)\mathbf{L}_1 = m\mathbf{a}_2^- + n(\mathbf{a}_2^- - \mathbf{a}_1^-). \quad (2.12)$$

In fact,  $\mathbf{L}_1$  and  $\mathbf{L}_2$  are primitive translations as long as  $m$  and  $n$  are coprime and  $|m - n|$  is not divisible by three [14]. Should  $|m - n|$  be a multiple of three, the primitive lattice vectors are instead given by [14]

$$\begin{aligned} \mathbf{L}_1 &= \frac{1}{3}(2n - m)\mathbf{a}_1^- + \frac{1}{3}(m - n)\mathbf{a}_2^-, \\ \mathbf{L}_2 &= \frac{1}{3}(n - m)\mathbf{a}_1^- + \frac{1}{3}(2m + n)\mathbf{a}_2^-. \end{aligned}$$

Intuitively, this difference in primitive lattice vectors occurs because for a given commensurate twist angle  $\theta$ , the angle  $\pi/3 - \theta$  is also commensurate and describes exactly the same lattice [13]. For  $|m - n| \nmid 3$ , it turns out that the integers  $m', n'$  with  $\Theta(m', n') = \pi/3 - \theta$  yield smaller lattice vectors in Eq. (2.11) than  $m, n$  do.

By some algebra, one finds the reciprocal lattice vectors for the case of  $|m - n| \nmid 3$  to be

$$\begin{aligned} \mathbf{G}_1 &= \frac{(m + n)m}{m^2 + n^2 + mn} \left( \frac{\mathbf{b}_1^-}{n} + \frac{\mathbf{b}_2^-}{m + n} \right), \\ \mathbf{G}_2 &= \frac{-mn}{m^2 + n^2 + mn} \left( \frac{\mathbf{b}_1^-}{m} - \frac{\mathbf{b}_2^-}{n} \right). \end{aligned}$$

The area of the moiré unit cell evaluates to

$$A_M = |\mathbf{L}_1 \times \mathbf{L}_2| = \frac{A_0|m-n|}{|2 \sin(\Theta(m,n)/2)|^2}, \quad (2.13)$$

$A_0 = \sqrt{3}a^2/2$  being the area of the graphene unit cell.

Since the period of the moiré lattice can become significantly larger than the unit cell of a graphene monolayer, the moiré Brillouin zone will usually be small in comparison to the monolayer Brillouin zone. This causes a Brillouin zone folding to take place, where multiple points in the monolayer Brillouin zone are mapped to the same point in the moiré Brillouin zone. In particular, for  $|m-n|=1$ , the Dirac points of the two monolayers are mapped to the  $\mathbf{K}$  and  $\mathbf{K}'$  points of the moiré Brillouin zone [15], where the bilayer consequently also becomes linearly dispersive.

## 2.3 Microscopic tight binding model

Up to on-site energies, the general form of the tight binding Hamiltonian is

$$\mathcal{H} = \sum_{i \neq j} \sum_{\sigma} t(\mathbf{R}_i - \mathbf{R}_j) c_{i\sigma}^{\dagger} c_{j\sigma}, \quad (2.14)$$

where  $\sum_{i \neq j}$  runs over all pairs of distinct atoms in the crystal lattice and  $\sum_{\sigma}$  is taken over the spin degree of freedom [2]. In addition,  $\mathbf{R}_i$  denotes the position of the atom at site  $i$  and  $t$  describes the hopping amplitude as a function of the interatomic separation. Since the coupling  $t$  is independent of the electronic spin, the sum over the spin degree of freedom will not affect the resulting eigenenergies and can be dropped. Considering a lattice with a basis consisting of multiple inequivalent atoms, the Hamiltonian can then be expressed as

$$\mathcal{H} = \sum_{X, X'} \sum_{\mathbf{L}, \mathbf{L}'} t((\mathbf{R}_X + \mathbf{L}) - (\mathbf{R}_{X'} + \mathbf{L}')) c^{\dagger}(\mathbf{R}_X + \mathbf{L}) c(\mathbf{R}_{X'} + \mathbf{L}') \quad (2.15)$$

where  $\sum_{\mathbf{L}}, \sum_{\mathbf{L}'}$  are taken over all lattice vectors and the indices  $X, X' = 1, \dots, B$  label the individual atoms in the crystal basis,  $B$  being the total number of atoms per unit cell. Here, we have defined  $t(\mathbf{0}) := 0$  such that on-site terms do not need to be explicitly excluded from the sum. Denote the number of moiré unit cells in the lattice by  $N_M$ . Introducing the Fourier



transform  $c^\dagger(\mathbf{R}) = \frac{1}{\sqrt{N_M}} \sum_{\mathbf{k}} e^{i\mathbf{k}\cdot\mathbf{R}} c^\dagger(\mathbf{k})$ , one then obtains

$$\begin{aligned} \mathcal{H} &= \frac{1}{N_M} \sum_{X,X'} \sum_{\mathbf{L},\mathbf{L}'} t((\mathbf{R}_X + \mathbf{L}) - (\mathbf{R}_{X'} + \mathbf{L}')) \sum_{\mathbf{k},\mathbf{k}'} e^{i\mathbf{k}\cdot(\mathbf{R}_X + \mathbf{L})} e^{-i\mathbf{k}'\cdot(\mathbf{R}_{X'} + \mathbf{L}')} c_X^\dagger(\mathbf{k}) c_{X'}(\mathbf{k}') \\ &= \frac{1}{N_M} \sum_{X,X'} \sum_{\mathbf{L},\mathbf{L}'} t(\mathbf{R}_X - (\mathbf{R}_{X'} + \mathbf{L}' - \mathbf{L})) \sum_{\mathbf{k},\mathbf{k}'} e^{i(\mathbf{k}-\mathbf{k}')\cdot\mathbf{L}} e^{i\mathbf{k}\cdot\mathbf{R}_X} e^{-i\mathbf{k}'\cdot(\mathbf{R}_{X'} + \mathbf{L}' - \mathbf{L})} c_X^\dagger(\mathbf{k}) c_{X'}(\mathbf{k}') \\ &= \sum_{X,X'} \sum_{\Delta\mathbf{L}} t(\mathbf{R}_X - (\mathbf{R}_{X'} + \Delta\mathbf{L})) \sum_{\mathbf{k}} e^{i\mathbf{k}\cdot\mathbf{R}_X} e^{-i\mathbf{k}\cdot(\mathbf{R}_{X'} + \Delta\mathbf{L})} c_X^\dagger(\mathbf{k}) c_{X'}(\mathbf{k}), \end{aligned}$$

where in the final equality, we have defined  $\Delta\mathbf{L} := \mathbf{L}' - \mathbf{L}$ , substituted  $\sum_{\mathbf{L},\mathbf{L}'} \rightarrow \sum_{\mathbf{L},\Delta\mathbf{L}}$ , and subsequently applied  $\sum_{\mathbf{L}} e^{-i(\mathbf{k}-\mathbf{k}')\cdot\mathbf{L}} = N_M \delta_{\mathbf{k}\mathbf{k}'}$ . Defining  $\Psi_{\mathbf{k}}^\dagger := (c_1^\dagger(\mathbf{k}), c_2^\dagger(\mathbf{k}), \dots, c_B^\dagger(\mathbf{k}))$ , this result can be expressed as

$$\mathcal{H} = \sum_{\mathbf{k}} \Psi_{\mathbf{k}}^\dagger h(\mathbf{k}) \Psi_{\mathbf{k}}, \quad (2.16)$$

where  $h(\mathbf{k})$  is a  $B \times B$  matrix with matrix elements

$$h^{XX'}(\mathbf{k}) := \sum_{\mathbf{L}} t(\mathbf{R}_X - (\mathbf{R}_{X'} + \mathbf{L})) e^{i\mathbf{k}\cdot(\mathbf{R}_X - (\mathbf{R}_{X'} + \mathbf{L}))}. \quad (2.17)$$

The matrix  $h(\mathbf{k})$  is commonly referred to as the Bloch Hamiltonian, and its eigenvalues determine the possible single-particle energies of an electron with wave vector  $\mathbf{k}$ .

Following Ref. [16], we assume that the hopping amplitude  $t$  is described by the commonly used Slater-Koster form for multilayer graphene [17],

$$t(\mathbf{R}) = -V_{pp\pi} e^{-(|\mathbf{R}|-a_0)/r_0} \left( 1 - \left( \frac{\mathbf{R} \cdot \mathbf{e}_z}{|\mathbf{R}|} \right)^2 \right) - V_{pp\sigma} e^{-(|\mathbf{R}|-d_0)/r_0} \left( \frac{\mathbf{R} \cdot \mathbf{e}_z}{|\mathbf{R}|} \right)^2, \quad (2.18)$$

where  $V_{pp\pi} = -2.7$  eV and  $V_{pp\sigma} = 0.48$  eV parametrize the strength of intra- and interlayer hopping, respectively. In addition,  $a_0 = 0.142$  nm is the nearest neighbour distance and  $d_0 = 0.335$  nm represents the interlayer distance. For the decay length  $r_0$ , we adopt a value of  $0.184a$  from Ref. [16], such that  $t(\mathbf{a}_i) = t_{\text{NNN}}$  for both of the graphene lattice vectors  $\mathbf{a}_i$ , with  $t_{\text{NNN}} = 0.1V_{pp\pi}$  being the next-to-nearest neighbour hopping amplitude for graphene. To restrict the number of non-zero matrix elements, the hopping amplitude is assumed to be negligibly small if the interatomic separation exceeds a value of  $6a_0$ , i.e.

$$t(\mathbf{R}) \approx 0 \text{ for } |\mathbf{R}| > 6a_0. \quad (2.19)$$

It is known from first-principles calculations [18] that the interlayer separation in a twisted graphene bilayer is not necessarily constant throughout the moiré unit cell, and instead differs between regions of AA and AB stacking. We account for such corrugation effects by adopting

the optimized interlayer distance

$$d(\boldsymbol{\delta}(\mathbf{r})) = \bar{d} + s \sum_{i=1}^3 \cos(\mathbf{b}_i \cdot \boldsymbol{\delta}(\mathbf{r})), \quad (2.20)$$

from Ref. [15], with the mean interlayer distance  $\bar{d} = 0.343$  nm, scaling  $s = 5.56$  pm and  $\mathbf{b}_3 := -\mathbf{b}_1 - \mathbf{b}_2$ . Here,  $\boldsymbol{\delta}(\mathbf{r}) = \mathcal{R}(\theta/2)\mathbf{r} - \mathcal{R}(-\theta/2)\mathbf{r}$  describes the local in-plane mismatch between the two monolayers, with  $|\boldsymbol{\delta}(\mathbf{r})| \approx 0$  in regions of AA stacking, and  $|\boldsymbol{\delta}(\mathbf{r})|$  reaching its maximum value in regions of AB stacking.

Note that even though we account for spatial variations in the interlayer distance, the parameter  $d_0$  in the Slater-Koster hopping Eq. (2.18) should not be adjusted for corrugation effects. Instead, corrugation is modelled by evaluating  $t$  for interatomic vectors  $\mathbf{R}$  with  $z$ -components of different magnitudes.

For a numerical calculation of the band structure, the matrix entries Eq. (2.17) are computed using the *C++* programming language. The resulting matrix is fed to a *Python* script with the help of the *pybind11* library [19]. Finally, the sparse matrix diagonalization capabilities of *Python's SciPy* library [20] are used to obtain the desired eigenvalues. Specifically, *SciPy* provides access to an implementation of the Implicitly Restarted Arnoldi Method [21], allowing one to determine a user-specified number of eigenvalues in the vicinity of a desired energy. Note that the time complexity of the Arnoldi method scales linearly with the dimension of the matrix [21]. Ramires and Lado [22] point out that for a calculation of the density of states, the Bloch matrix need not be diagonalized, and one can instead apply the more efficient Kernel polynomial method.

## 2.4 Continuum model

At small twist angles, the unwieldy tight binding Hamiltonian introduced above is well approximated by the computationally simpler Bistritzer-MacDonald Hamiltonian, providing a heuristic description of the physics of TBG based on a continuum model for monolayer graphene. The Bistritzer-MacDonald Hamiltonian allows for the computation of moiré bands at a computational cost that is independent of the system's twist angle. In addition, it can even serve as a starting point for entirely analytic studies of TBG [5, 23]. Generalizations of the Bistritzer-MacDonald model that describe the physics of TBG in the vicinity of arbitrary commensurate twist angles, or extend the Bistritzer-MacDonald Hamiltonian to commensurate structures besides TBG have since also been proposed [13, 14].

At small commensurate twist angles, the Bistritzer-MacDonald model reproduces the dispersion of the microscopic Hamiltonian near charge neutrality to a good degree of accuracy (see Fig. 2.6 for some direct comparisons), with the additional benefit of being immediately applicable to incommensurate twist angles. However, the model necessitates an effective treatment

of Coulomb interactions, where interactions are projected into a set of active bands near the Fermi energy. In addition, it does not provide an accurate description of the remote bands and is not capable of reproducing all features of the microscopic dispersion (see Section 2.6).

A derivation heavily based on Refs. [2, 15] is given below for the convenience of the reader. By expanding the Bloch Hamiltonian of monolayer graphene to first order around either of the Dirac points  $\mathbf{K}_\xi$ ,  $\xi = \pm 1$ , one obtains the continuum Hamiltonian

$$H_\xi(\mathbf{k}) = v_F(\mathbf{k} - \mathbf{K}_\xi) \cdot (\xi\sigma_x, \sigma_y). \quad (2.21)$$

Here,  $v_F$  is the Fermi velocity at the systems Dirac points, i.e. the effective velocity of an electron with wave vector  $\mathbf{k} \approx \mathbf{K}_\xi$ . The Pauli matrices  $\sigma_x$ ,  $\sigma_y$  are taken to act on sublattice space and  $\xi$  is termed the valley index. The Hamiltonian  $H_\xi^\ell$ ,  $\ell = \pm 1$  of a monolayer with a twist angle of  $\ell \cdot \theta/2$  is then obtained by substituting  $\mathbf{k} - \mathbf{K}_\xi \rightarrow \mathcal{R}(-\ell \cdot \theta/2)(\mathbf{k} - \mathbf{K}_\xi)$  in Eq. (2.21). In layer space, the full effective Hamiltonian of the twisted bilayer in valley  $\xi$  is thus given by

$$\mathcal{H}_\xi^{\text{BM}}(\mathbf{k}) = \begin{pmatrix} H_\xi^-(\mathbf{k}) & U^\dagger \\ U & H_\xi^+(\mathbf{k}) \end{pmatrix},$$

with the effective interlayer coupling  $U$ .

To proceed, the key insight is that locally, the in-plane mismatch of the two monolayers can be understood as an in-plane translation  $\boldsymbol{\delta}$ , as opposed to an actual rotation. Globally, we can then approximate the layer mismatch by making the displacement  $\boldsymbol{\delta}$  depend on position according to

$$\boldsymbol{\delta}(\mathbf{r}) = \mathcal{R}(\theta/2)\mathbf{r} - \mathcal{R}(-\theta/2)\mathbf{r}.$$

A useful expression for the interlayer coupling is obtained by first considering only the case of constant  $\boldsymbol{\delta}$  and subsequently replacing  $\boldsymbol{\delta} \rightarrow \boldsymbol{\delta}(\mathbf{r})$  in the result. The error introduced by this substitution is assumed to be tolerable for sufficiently small twist angles, where the position dependence of  $\boldsymbol{\delta}(\mathbf{r})$  will be very slow.

Introducing a combined sublattice and layer index  $X$ , the matrix elements of the interlayer coupling matrix are given by  $U_{XX'}(\mathbf{k}) = \langle \mathbf{k}X | \mathcal{H} | \mathbf{k}X' \rangle$ , where  $|\mathbf{k}X\rangle = c_X^\dagger(\mathbf{k})|0\rangle$  and  $\mathcal{H}$  is the tight binding Hamiltonian for the bilayer with constant displacement  $\boldsymbol{\delta}$ . The tight binding Hamiltonian has the form of Eq. (2.15) with four atoms per unit cell, i.e. the summation indices  $X$  and  $X'$  in Eq. (2.15) run over the values A1, B1, A2, and B2. Note that the lattice vectors of the displaced bilayer coincide with the monolayer lattice vectors. The matrix element can be evaluated using a calculation that is analogous to the derivation of Eq. (2.17),

yielding

$$U_{XX'}(\mathbf{k}) = \sum_{\mathbf{L}} t(\mathbf{R}_X - (\mathbf{R}_{X'} + \mathbf{L}')) e^{-i\mathbf{k} \cdot (\mathbf{R}_X - (\mathbf{R}_{X'} + \mathbf{L}'))}.$$

Here, the displacement between the lattice sites can be expressed as  $\mathbf{R}_X - \mathbf{R}_{X'} = \boldsymbol{\tau}_{XX'} + \boldsymbol{\delta} + d(\boldsymbol{\delta})\mathbf{e}_z$ , with the interlayer distance  $d$  given by Eq. (2.20), and

$$\begin{pmatrix} \boldsymbol{\tau}_{A2,A1} & \boldsymbol{\tau}_{A2,B1} \\ \boldsymbol{\tau}_{B2,A1} & \boldsymbol{\tau}_{B2,B1} \end{pmatrix} = \begin{pmatrix} 0 & \boldsymbol{\delta}_1 \\ -\boldsymbol{\delta}_1 & 0 \end{pmatrix},$$

where the nearest neighbour vector  $\boldsymbol{\delta}_1$  is defined in Eq. (2.1). Exploiting that  $\mathbf{k} \cdot \mathbf{e}_z = 0$ , we thus have

$$U_{XX'}(\mathbf{k}) = \sum_{\mathbf{L}} t(\mathbf{L} + \boldsymbol{\tau}_{XX'} + \boldsymbol{\delta} + d(\boldsymbol{\delta})\mathbf{e}_z) e^{-i\mathbf{k} \cdot (\mathbf{L} + \boldsymbol{\tau}_{XX'} + \boldsymbol{\delta})}.$$

This function must be periodic in the displacement  $\boldsymbol{\delta}$ , since a further shift  $\boldsymbol{\delta} \rightarrow \boldsymbol{\delta} + \mathbf{L}'$  by a lattice vector  $\mathbf{L}'$  of the bilayer can always be absorbed into  $\mathbf{L}$ , and  $d$  is periodic under lattice translations. We can thus Fourier expand the matrix elements as

$$U_{XX'}(\mathbf{k}) = \sum_{\mathbf{G}} \tilde{U}_{XX'}(\mathbf{G}, \mathbf{k}) e^{i(\boldsymbol{\delta} + \boldsymbol{\tau}_{XX'}) \cdot \mathbf{G}},$$

with Fourier coefficients

$$\begin{aligned} \tilde{U}_{XX'}(\mathbf{G}, \mathbf{k}) &= \frac{1}{A_0} \int_{\text{UC}} \sum_{\mathbf{L}} t(\mathbf{L} + \mathbf{R} + d(\mathbf{R} - \boldsymbol{\tau}_{XX'})\mathbf{e}_z) e^{-i\mathbf{k} \cdot (\mathbf{L} + \mathbf{R})} e^{-i\mathbf{G} \cdot \mathbf{R}} d^2\mathbf{R} \\ &= \frac{1}{A_0} \sum_{\mathbf{L}} \int_{\text{UC}} t(\mathbf{L} + \mathbf{R} + d(\mathbf{L} + \mathbf{R} - \boldsymbol{\tau}_{XX'})\mathbf{e}_z) e^{-i\mathbf{k} \cdot (\mathbf{L} + \mathbf{R})} e^{-i\mathbf{G} \cdot (\mathbf{L} + \mathbf{R})} d^2\mathbf{R} \\ &= \frac{1}{A_0} \int_{\mathbb{R}^2} t(\mathbf{R} + d(\mathbf{R} - \boldsymbol{\tau}_{XX'})\mathbf{e}_z) e^{-i(\mathbf{k} + \mathbf{G}) \cdot \mathbf{R}} d^2\mathbf{R}. \end{aligned}$$

Here,  $A_0$  is the area of the bilayer unit cell, and  $\int_{\text{UC}}$  denotes integration over a unit cell of the bilayer (which coincides with the monolayer unit cell).

To generalize to a twisted bilayer, we substitute  $\boldsymbol{\delta} \rightarrow \boldsymbol{\delta}(\mathbf{r})$  as explained above, and additionally insert  $\mathbf{k} \approx \mathbf{K}_\xi$ , such that the integral need not be evaluated numerically for all  $\mathbf{k}$ . In the Bistritzer-MacDonald model, the Fourier expansion is then truncated at the three largest components, after some algebra yielding

$$U(\mathbf{r}) = \begin{pmatrix} u & u' \\ u' & u \end{pmatrix} + \begin{pmatrix} u & u'\omega^{-\xi} \\ u'\omega^\xi & u \end{pmatrix} e^{i\xi\mathbf{G}_1 \cdot \mathbf{r}} + \begin{pmatrix} u & u'\omega^\xi \\ u'\omega^{-\xi} & u \end{pmatrix} e^{i\xi(\mathbf{G}_1 + \mathbf{G}_2) \cdot \mathbf{r}},$$

with  $\omega = e^{2\pi i/3}$ , and

$$u = \frac{1}{A_0} \int t(\mathbf{R} + d(\mathbf{R})\mathbf{e}_z) e^{-i\mathbf{K}_\xi \cdot \mathbf{R}}, \quad (2.22)$$

$$u' = \frac{1}{A_0} \int t(\mathbf{R} + d(\mathbf{R} - \boldsymbol{\delta}_1)\mathbf{e}_z) e^{-i\mathbf{K}_\xi \cdot \mathbf{R}}. \quad (2.23)$$

With this result for  $U(\mathbf{r})$  in hand, one can substitute  $\mathbf{r} \rightarrow i\nabla$  and numerically solve the Schrödinger equation

$$H_\xi^{\text{BM}}(\mathbf{k})\psi_{\xi\mathbf{k}}(\mathbf{r}) = \varepsilon_{\mathbf{k}}\psi_{\xi\mathbf{k}}(\mathbf{r}), \quad (2.24)$$

with  $\psi_{\xi\mathbf{k}}$  a four component spinor. For a suitable choice of coefficients  $c_{\xi\mathbf{k}}^X$ , we have by Bloch's theorem

$$\psi_{\xi\mathbf{k}}^X(\mathbf{r}) = e^{i\mathbf{k} \cdot \mathbf{r}} \sum_{\mathbf{G}} c_{\xi\mathbf{k}}^X(\mathbf{G}) e^{i\mathbf{G} \cdot \mathbf{r}}, \quad (2.25)$$

but the series expansion can be truncated: At sufficiently small twist angles, the Dirac points  $\mathbf{K}_{-, \ell}$  ( $\mathbf{K}_{+, \ell}$ ) of the two layers  $\ell = \pm 1$  are rotated only slightly with respect to one another. Hence, the corresponding valleys are located almost on top of one another, creating an effective  $\mathbf{K}_-$  ( $\mathbf{K}_+$ ) valley of the bilayer [15]. The low energy spectrum is dominated by hybridized graphene eigenstates in this bilayer valley, corresponding to terms  $\mathbf{k} + \mathbf{G} \approx \mathbf{K}_\xi$  in Eq. (2.25), and the remaining wavevectors can be discarded. Specifically, in Ref. [15], only terms in the cutoff circle

$$|(\mathbf{k} + \mathbf{G}) - \mathbf{q}_0| < n|\mathbf{G}_1| \quad (2.26)$$

are retained, where  $n = 4$  is an arbitrary threshold and  $\mathbf{q}_0 = (\mathbf{K}_{\xi,-} + \mathbf{K}_{\xi,+})/2$  is the center of valley  $\xi$  in the bilayer. Here, we instead choose a value of  $n = 5$ , since this impacts the results obtained for the Fermi velocity at small twist angles (see Section 2.8). Inserting the truncated expansion into Eq. (2.24), one ends up with a finite dimensional eigenvalue problem that we solve numerically with the help of *Python's NumPy* library. The *Python* source code is based on a *Mathematica* implementation provided in Ref. [2].

A prerequisite for the numerical diagonalization is that appropriate values for the interlayer coupling strengths  $u$ ,  $u'$  have been determined. The corresponding integrals Eq. (2.22) can be carried out numerically, and with the help of the *Mathematica* software we obtain  $u = u' = 0.0903$  eV when assuming a constant interlayer separation of  $\bar{d} = 0.343$  nm. In the presence of corrugation effects, intra- and inter-sublattice coupling differ, with  $u = 0.0797$  eV,  $u' = 0.0975$  eV.

For consistency with the microscopic model, the monolayer Fermi velocity  $v_F^0$  in Eq. (2.21)

is computed using a tight binding model with the hopping amplitude Eq. (2.18) and cut-off threshold Eq. (2.19), yielding  $v_F^0 = 1.36a_0t/\hbar$ . This is slightly lower than the value of

$$v_F^0 = 3\frac{a_0t}{2\hbar} \approx \frac{c}{300}$$

obtained when considering only the nearest neighbour hopping  $t = 2.7$  eV.

## 2.5 Approximation of incommensurate twist angles

One limitation of the microscopic tight binding model is its lack of applicability to configurations that are not rigorously periodic. In an attempt to lift this constraint, we show here that all incommensurate configurations, although not exactly periodic, can be approximated to arbitrary precision by finding suitable commensurate twist angles. However, the approximation scheme described here turns out to be difficult to implement in practice.

Recall that all commensurate twist angles can be enumerated using the expression  $\Theta(m, n)$  given by Eq. (2.10). Since  $\Theta(m, n)$  is symmetric under exchange of  $m$  and  $n$ , we may assume without loss of generality that  $n < m$ . To simplify the expression enumerating the commensurate twist angles, we can thus substitute  $n = s \cdot m$  with  $s \in [0, 1] \cap \mathbb{Q}$  in 2.10. All occurrences of  $m$  cancel out, and the commensurate twist angles are then given by

$$\Theta(s) = \arccos\left(\frac{1}{2} \frac{1 + s^2 + 4s}{1 + s^2 + s}\right)$$

for arbitrary  $s \in [0, 1] \cap \mathbb{Q}$ . An incommensurate twist angle  $\theta$  can thus be approximated to arbitrary precision as  $\theta \approx \Theta(s')$ , where  $s' \in [0, 1] \cap \mathbb{Q}$  is a sufficiently accurate rational approximation of  $s = \Theta^{-1}(\theta)$ . The inverse function  $\Theta^{-1}$  is well defined, and by tedious algebra one obtains

$$\Theta^{-1}(\theta) = \frac{\sqrt{3}|\sin\theta| + \cos\theta - 2}{1 - 2\cos\theta}.$$

The corresponding integers  $m, n \in \mathbb{N}$  specifying the lattice vectors of the commensurate lattice according to Eq. (2.11) can then be determined by expressing  $s'$  as an irreducible fraction  $\frac{n}{m} = s'$ .

However, there are two obstructions that result in this approximation scheme being hardly suitable for practical applications: First, the size of the commensurate moiré unit cell Eq. (2.13) depends on the difference  $|m - n|$ , meaning that a more accurate approximation of the twist angle will also result in a larger unit cell, and hence a higher dimensional Bloch Hamiltonian. Consequently, the computational cost of diagonalizing the Hamiltonian can be expected to increase by a factor of  $|m - n|$  due to the linear time complexity of the Arnoldi method.

Second, Eq. (2.13) also results in the size of the moiré Brillouin zone shrinking as the approx-

imation becomes more accurate. More specifically, the tight binding Brillouin zone will be smaller than the continuum model Brillouin zone by a factor of  $|m - n|$ , and a direct comparison with the continuum model will involve unfolding the tight binding band structure into the larger continuum model Brillouin zone.

For these reason, we limit ourselves to using only the set of commensurate twist angles with  $|m - n| = 1$  in the remainder of the text. In particular, this means that the moiré Brillouin zone coincides with the Brillouin zone in the continuum model, and the resulting band structures are directly comparable. In the vicinity of the magic angle, the moiré unit cells under consideration then contain roughly 11 000 atoms.

## 2.6 Electronic band structure

We begin our discussion of the properties of the two Hamiltonians with some general features of the band structures they predict. Some of these are best illustrated by the Brillouin zone cross sections Fig. 2.6:

1. At small twist angles, one observes the emergence of four weakly dispersive *flat* bands around charge neutrality [5]. From the continuum description, we can infer that these bands are labeled by different valley indices  $\xi = \pm 1$ . In the vicinity of either Dirac point, the continuum description of the flat bands is in good agreement with the microscopic model. Farther away and in the *remote* bands, deviations between the two models occur.
2. The typical energy scale of the bands appears to decrease with the twist angle. This is a result of energy bands being folded as the moiré Brillouin decreases in size.
3. Along the paths  $\mathbf{K} - \mathbf{\Gamma}$  and  $\mathbf{M} - \mathbf{K}'$ , the four flat bands reduce to two groups of degenerate bands, with the bands within each group differing only by their valley indices. This degeneracy is lifted along the path  $\mathbf{\Gamma} - \mathbf{M}$ . The occurrence of degeneracies along parts of the Brillouin zone is a consequence of the  $C_2$  and  $C_3$  symmetries of the Hamiltonian. Similar behaviour is apparent in the remote bands.
4. Neither the continuum nor the microscopic band structure is symmetric under exchange of electrons and holes. This is particularly noticeable in Fig. 2.6c.

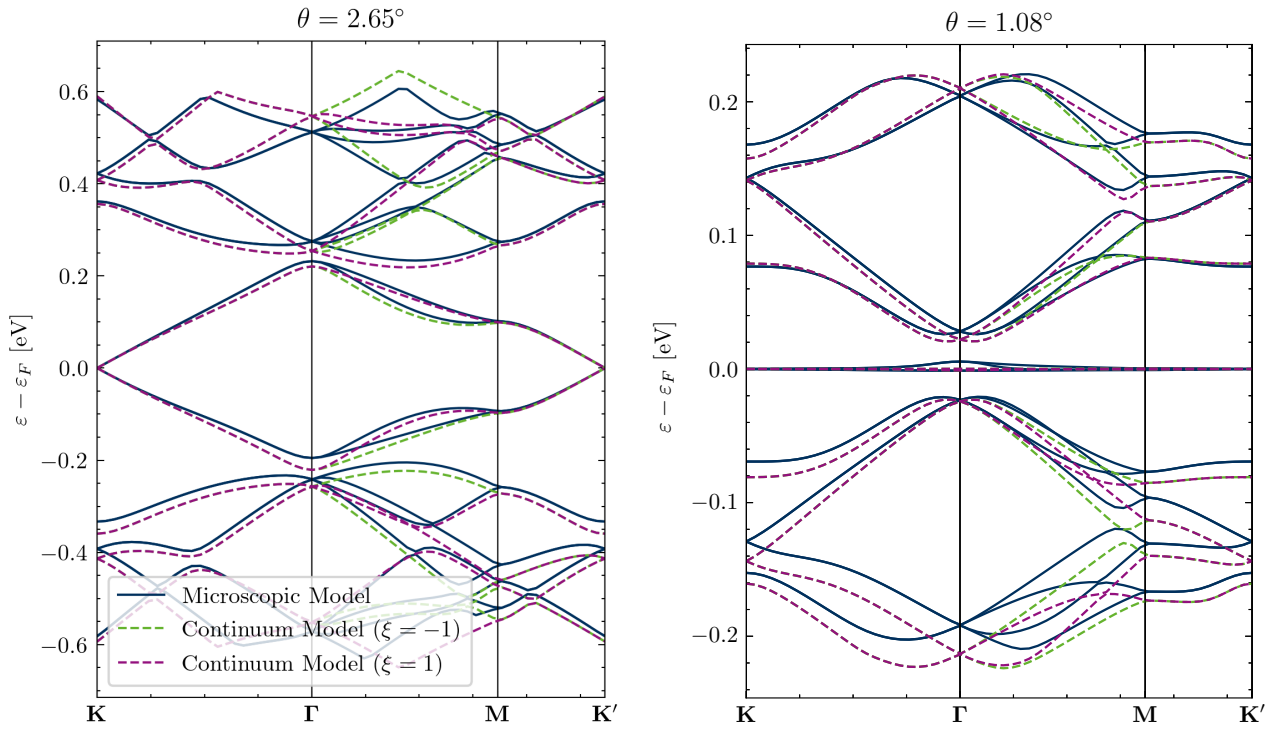
We note that in the microscopic model, these features are not necessarily present for the case of  $|m - n| > 1$  in Eq. (2.11) due to the effects of Brillouin zone folding.

Additional insights can be gained from an inspection of the contour plots Fig. 2.7. To limit the computational expense, these were computed only for the continuum Hamiltonian.

1. The dispersion in the flat bands forms a pattern with threefold rotational symmetry resembling a tripod<sup>2</sup>. The tripods of the two flat conduction bands are rotated by 180°

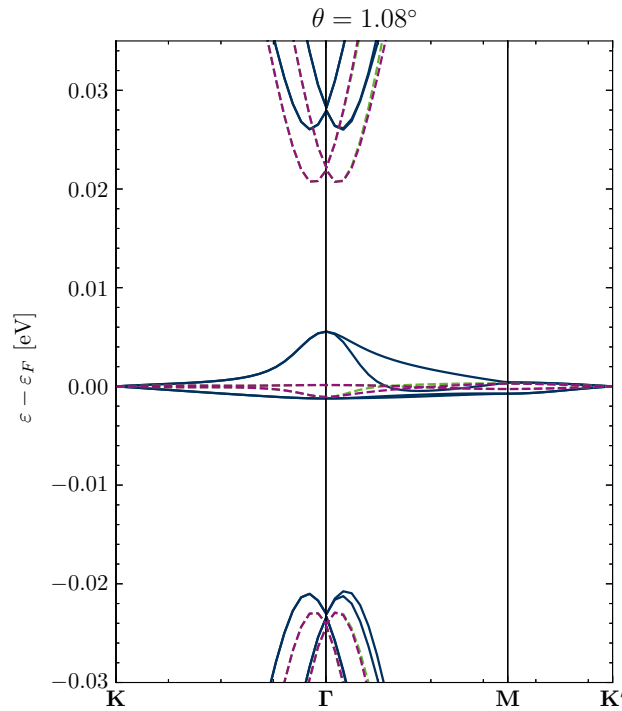
---

<sup>2</sup>It appears that this label was introduced by Bernevig et al. [23] with their aptly named tripod model.



(a) Energy bands for a twist angle of  $\Theta(12, 13) = 2.65^\circ$ .

(b) Energy bands for a twist angle of  $\Theta(30, 31) = 1.08^\circ$ .



(c) Close-up view of the flat bands for a twist angle of  $\Theta(30, 31) = 1.08^\circ$ .

**Figure 2.6:** Comparison of band structures predicted by the continuum and microscopic model.



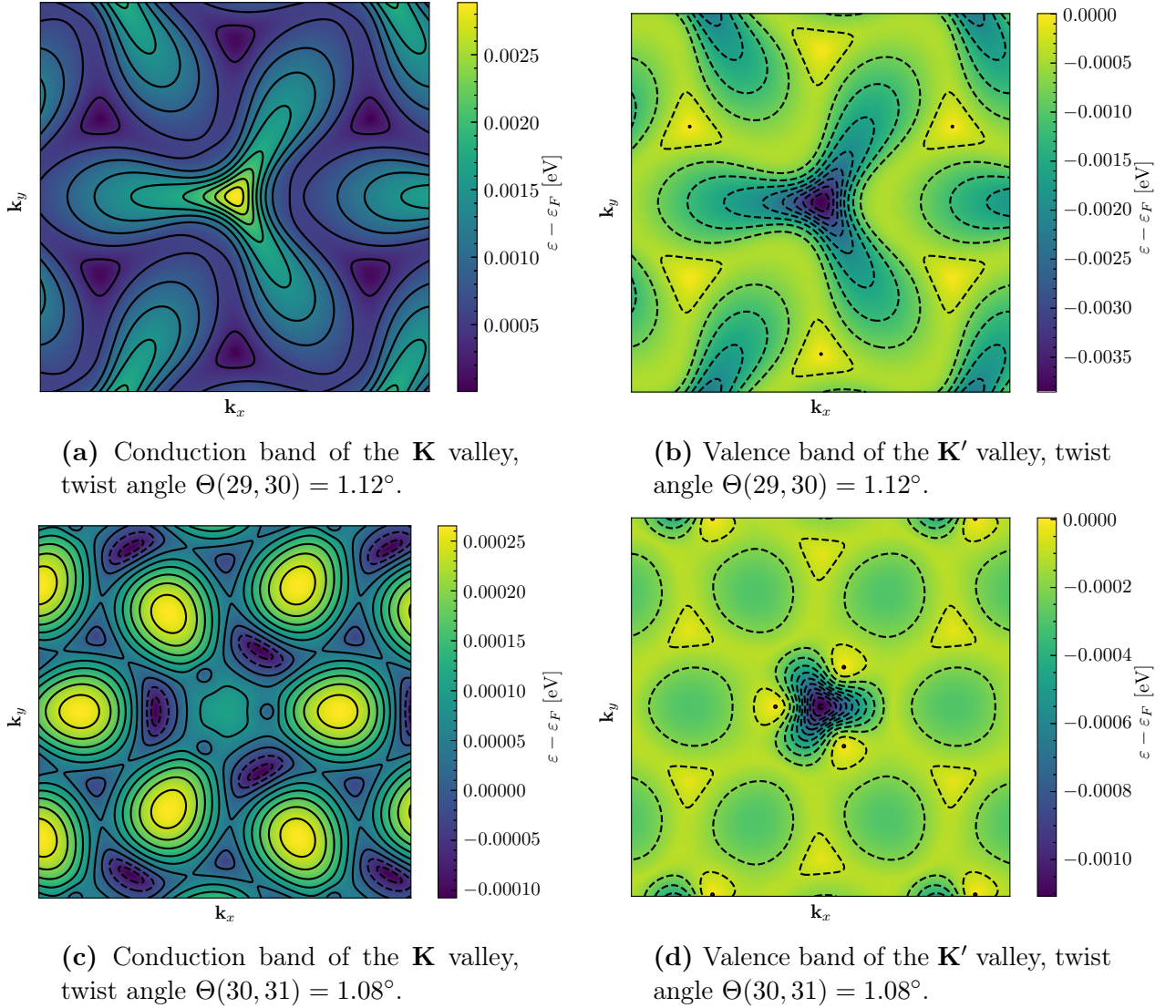


**Figure 2.7:** Contour plots of the flat bands in the continuum model. Dashed lines correspond to contours below the Fermi energy.

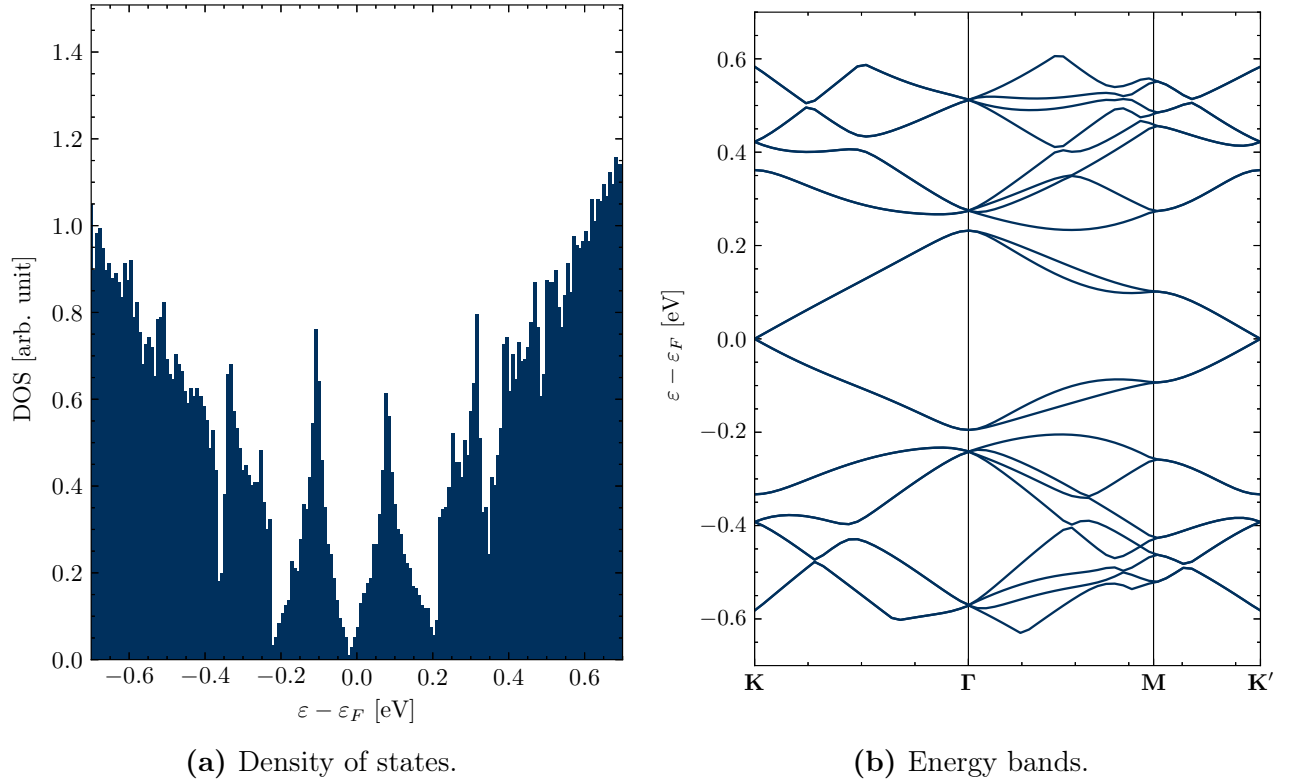
with respect to one another, but their dispersion is otherwise identical. The same applies to the two flat valence bands.

2. The minimum band separation always occurs at the  $\mathbf{K}$  and  $\mathbf{K}'$  points, where the conduction bands and valence bands touch. Intuitively, this happens because the Dirac points of monolayer graphene are always folded onto the  $\mathbf{K}$  and  $\mathbf{K}'$  points of the bilayer, as was discussed in Section 2.2.
3. For twist angles of  $1.08^\circ \lesssim \theta \lesssim 1.10^\circ$ , there occurs a transition in the continuum model dispersion, during which the flat bands no longer resemble the tripod shape. This is illustrated in Fig. 2.7. The tripods in a given band on either side of the transition are rotated by  $180^\circ$  with respect to one another. It is also apparent in Fig. 2.7c that during the transition, the continuum dispersion develops a Fermi surface and should thus become metallic. Since we did not observe similar behaviour with the microscopic Hamiltonian, we assume this result is an artifact of the continuum model in use here. For instance, the transition could be a result of the truncation of the Fourier expansion for the interlayer coupling matrix.
4. All four bands appear to reach their maximum distance to the Fermi level, and hence also the maximum band separation, at the  $\mathbf{\Gamma}$  point. This is not only the largest direct separation, but also the maximum indirect band width of the flat bands. An exception to this behaviour occurs during the above mentioned transition in the continuum model, where the maximum band separation is instead shifted towards the  $\mathbf{M}$  point.

The first of these properties can be understood as a consequence of the time reversal symmetry of the TBG Hamiltonian: In the continuum model, the two flat conduction bands are generated by different valleys. Time reversal exchanges the two valleys and maps  $\mathbf{k} \rightarrow -\mathbf{k}$ , thus yielding  $\varepsilon_{n,\xi}(\mathbf{k}) = \varepsilon_{n,-\xi}(-\mathbf{k})$ , where  $n$  is the band index [24]. At sufficiently small twist angles, the low energy bands in the microscopic model are also approximately valley polarized (see Fig. 3.5), and this argument remains applicable.

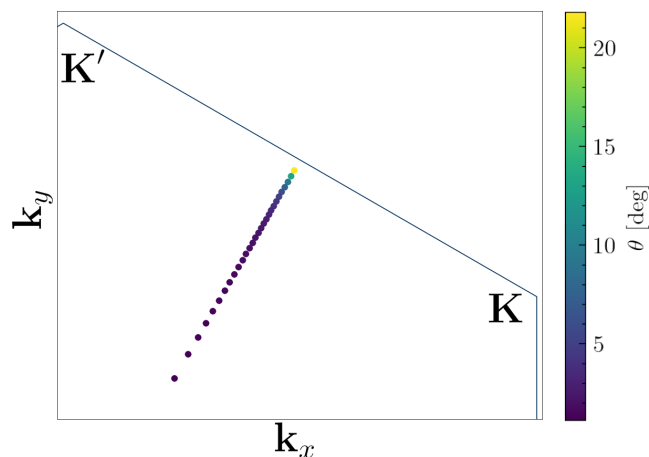
## 2.7 Density of states and Van Hove singularities

Fig. 2.8 illustrates the density of states for a fixed twist angle of  $\theta = 2.65^\circ$ . Similarly to the monolayer dispersion, one observes a vanishing density of states at the Fermi energy, as well as the presence of two pronounced Van Hove peaks close to the Fermi energy. The energy separation of these peaks turns out to be a deciding factor for the emergence of correlated states of matter in TBG, with the two Van Hove singularities merging at the magic angle [3]. Due to the connection between Van Hove singularities and saddle points in the electronic dispersion, it is thus important to gain an understanding of the evolution of the low energy saddle points as a function of the system's twist angle.



**Figure 2.8:** Density of states and corresponding energy bands in the microscopic model for a twist angle of  $\Theta(12, 13) = 2.65^\circ$ . The density of states was computed by sampling the dispersion at 1121 regularly spaced points in the Brillouin zone. The energy bands shown here are identical to those in Fig. 2.6a.

In order to investigate the qualitative behaviour of saddle points in the TBG dispersion, we locate critical points in the Brillouin zone by means of the finite difference approximation. Since only a discrete set of commensurate angles need to be considered, a classification of critical points into extrema and saddle points can subsequently be carried out manually by inspecting the local contour lines. To limit the computational expense, this calculation is carried out only in the continuum model, under the assumption that the behaviour changes only slightly for the microscopic model. Note that this assumption may not be warranted at all twist angles. Specifically, Fig. 2.6c shows qualitative differences between the flat bands of the two models at a twist angle of  $1.08^\circ$ , where, as discussed above, the continuum model exhibits an unusual dispersion. In addition, the finite difference computation was found to be lacking in accuracy for a quantitative investigation, and depending on the twist angle, different techniques need to be used instead. We will elaborate on these below.



**Figure 2.9:** Evolution of the saddle point location for the  $\xi = 1$  flat conduction band as a function of the twist angle  $\theta > \theta_C$ . For illustrative purposes, the lattice vectors at different twist angles are scaled such that all Brillouin zones have the same size.

The evolution of the saddle points is characterized by the presence of a critical twist angle  $\theta_C \approx \Theta(30, 31) = 1.08^\circ$  at which a topological transition occurs [25]:

- For  $\theta > \theta_C$ , the interplay of the tripods of adjacent Brillouin zones (see Fig. 2.7) causes the emergence of saddle points in the moiré Brillouin zone along three of the  $\Gamma - \mathbf{M}$  paths. As the twist angle is decreased, these points shift closer to the  $\Gamma$  point. In this respect, TBG differs from monolayer graphene, where saddle points are instead located at all six  $\mathbf{M}$  points. The finite difference computation indicates that along the one dimensional  $\Gamma - \mathbf{M}$  paths, saddle points manifest as local minima. Hence, their precise location can be determined by numerical minimization along said paths. The results are illustrated in Fig. 2.9.
- For  $\theta < \theta_C$ , Fig. 2.10 demonstrates how the number of saddle points increases due to the emergence of additional local extrema in the moiré Brillouin zone. Here, the precise

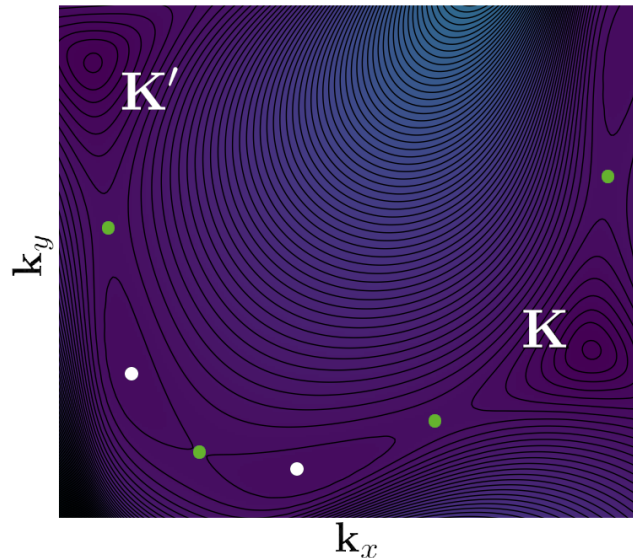


**Figure 2.10:** At a critical twist angle  $\theta_C$ , the emergence of additional local extrema in the TBG dispersion causes the number of saddle points to increase. Approximate locations of the saddle points and emergent extrema in the contour plot are highlighted in green and white, respectively.

location of saddle points is determined manually by searching for intersections in the contour lines of the spectrum close to the approximate critical point locations resulting from the finite difference computation. Naturally, some remaining amount of error is unavoidable with this manual approach. There appears to be no clear pattern to the total number of saddle points in the flat bands below  $\theta_C$ , but the number of saddle points tends to increase further as the twist angle is being decreased.

The properties of the low energy Van Hove singularities, as well as the associated saddle points, have been the subject of a number of studies in the literature [25–27]. Notably, Ref. [25] investigates the topological transition associated with a change in the number of saddle points using a phenomenological polynomial ansatz for the local dispersion. In Ref. [26], properties of the saddle points are instead deduced from a perturbative expansion of the low energy spectrum in the continuum model.

## 2.8 Band separation and Fermi velocity

Of particular interest to the physics of TBG are magic twist angles where the two Van-Hove singularities near charge neutrality merge, stimulating the occurrence of electron-electron interactions [3]. Here, we determine the largest magic angle by directly computing the energy separation of saddle points in the moiré Brillouin zone. As discussed in the previous section, finding the location of saddle points in the spectrum poses a numerical challenge, and a common alternative approach is to instead label twist angles as magical if they minimize the system’s Fermi velocity [5]. Since the Fermi velocity serves as an indicator for band flatness, this is

expected to yield similar results for the location of the magic angle. We thus supplement our result by an investigation of the Fermi velocity as a function of the twist angle. We additionally compute the band separation at charge neutrality at the  $\Gamma$  point, where the deviation between the continuum and microscopic model tends to be largest.

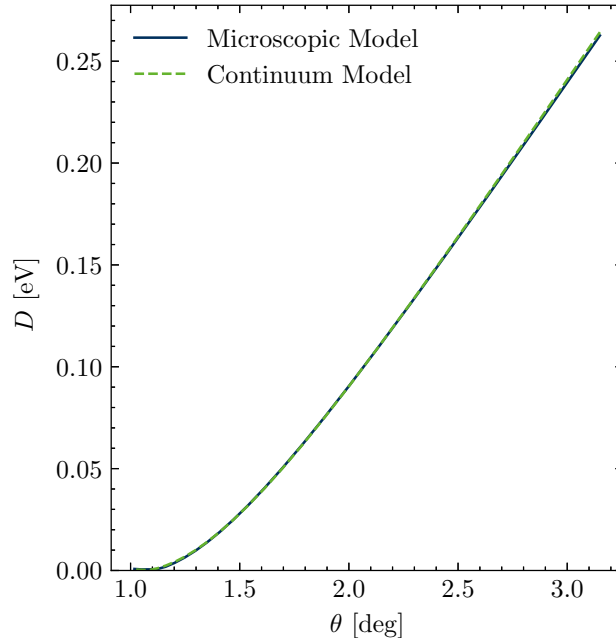
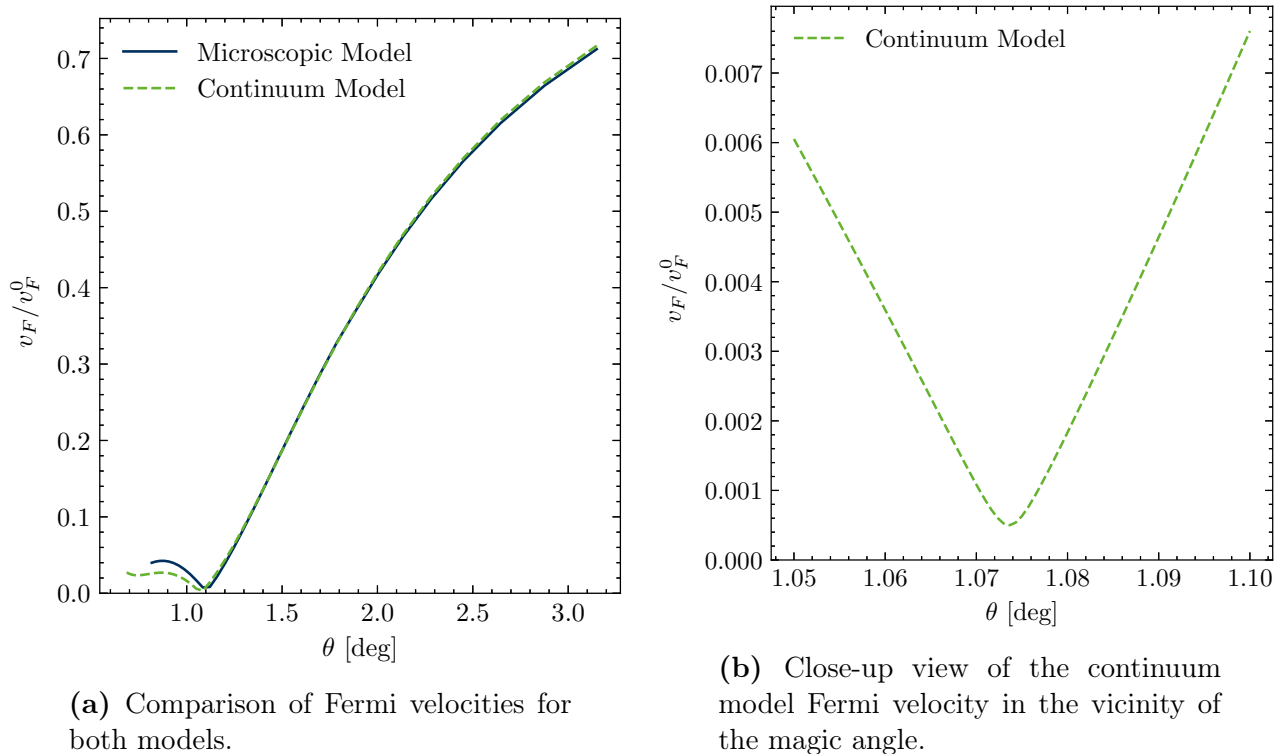


**Figure 2.11:** Energy separation of the flat valence and conduction bands at their saddle points. At twist angles where multiple saddle points at different energies exist, the minimum of all indirect band gaps between saddle points is shown.

Results for the saddle point energy separation are shown in Fig. 2.11. The computation is based on the saddle point locations determined in the previous section, and thus potential inaccuracies in the saddle point locations propagate into this computation. Evidently, the predictions of both models agree remarkably well and the energy separation initially decreases with the twist angle. Both models take on a local minimum at an angle of approximately  $1^\circ$ , although the precise locations of their first magic angles differ: In the microscopic model, the minimum separation occurs at  $\theta_m \approx \Theta(31, 32) = 1.05^\circ$ , whereas the continuum model predicts a magic angle of  $\theta_m \approx \Theta(30, 31) = 1.08^\circ$ .

The Fermi velocity is computed for each of the four flat bands by means of a finite difference approximation along the direction  $\mathbf{K} - \Gamma$  in the first Brillouin zone<sup>3</sup>. The results are similar in magnitude for all four bands, and the corresponding average velocity at different twist angles is shown in Fig. 2.12 for both the continuum and microscopic model. A minimum is located at the first magic angle of  $\theta_m \approx \Theta(30, 31) = 1.08^\circ$  for the microscopic model and  $\theta_m = 1.074^\circ$  for the continuum model. The Fermi velocity remains finite even at the magic angle, where it takes on a value of roughly  $0.004v_F^0 \approx 10^{-5}c$  for the microscopic Hamiltonian. In general, the predictions

<sup>3</sup>Since the contour lines around the  $\mathbf{K}_\xi$  points resemble circles (see Fig. 2.10), the Fermi velocity should be independent of the direction along which the derivative is computed.



(a) Comparison of Fermi velocities for both models.

(b) Close-up view of the continuum model Fermi velocity in the vicinity of the magic angle.

**Figure 2.12:** Bilayer Fermi velocity along the path  $\mathbf{K} - \mathbf{\Gamma}$  as a fraction of the single-layer Fermi velocity.

of both models agree remarkably well, with obvious deviations occurring only below the magic angle. Similar results for the Fermi velocity have been reported in the literature [5, 14, 18, 28], though exact numerical values appear to be sensitive to the parameters of the model.

When studying correlated phases in TBG, it is additionally useful to have an understanding of the dependence of the magic angle condition on the strength of the interlayer coupling. The coupling strength  $V_{pp\sigma}$  in Eq. (2.18) that minimizes the Fermi velocity at a given twist angle is illustrated in Fig. 2.13. Notice how for small twist angles, the two quantities depend linearly on each other. Additionally, the required interlayer coupling is consistently larger in the presence of corrugation effects. Phrased differently, variations in the interlayer spacing lead to a reduction of the magic angle for any given coupling strength.

Small but more frequent deviations between the two models occur in the  $\mathbf{\Gamma}$  point band separation, i.e. the energy separation between the two (locally degenerate) flat conduction and valence bands at the  $\mathbf{\Gamma}$  point as a function of the twist angle. The values obtained for both models are shown in Fig. 2.14, with two local minima occurring in the domain under consideration. Unlike the Fermi velocity, the band separation in the continuum model appears to vanish completely at a twist close to, but slightly different from, the magic angle. This observation does not imply that the bands become perfectly flat: Rather, the location of maximum band separation is shifted from the  $\mathbf{\Gamma}$  point to the  $\mathbf{M}$  point for angles close to the magic angle, as alluded to in Section 2.6.

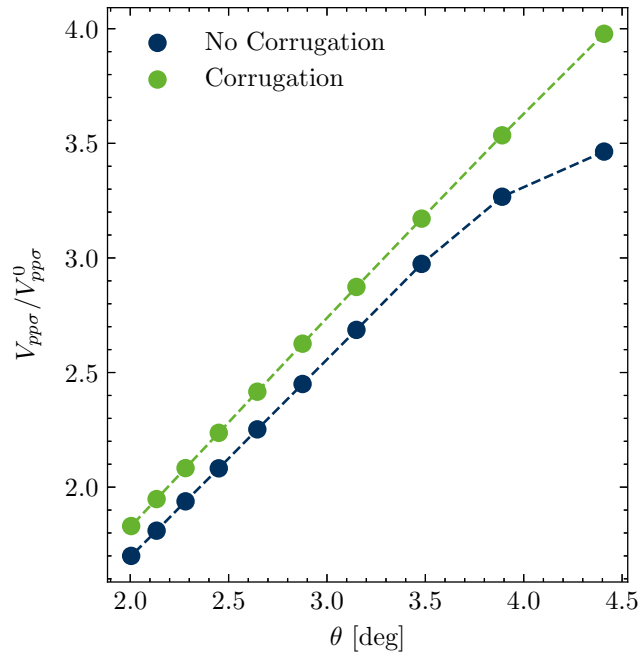
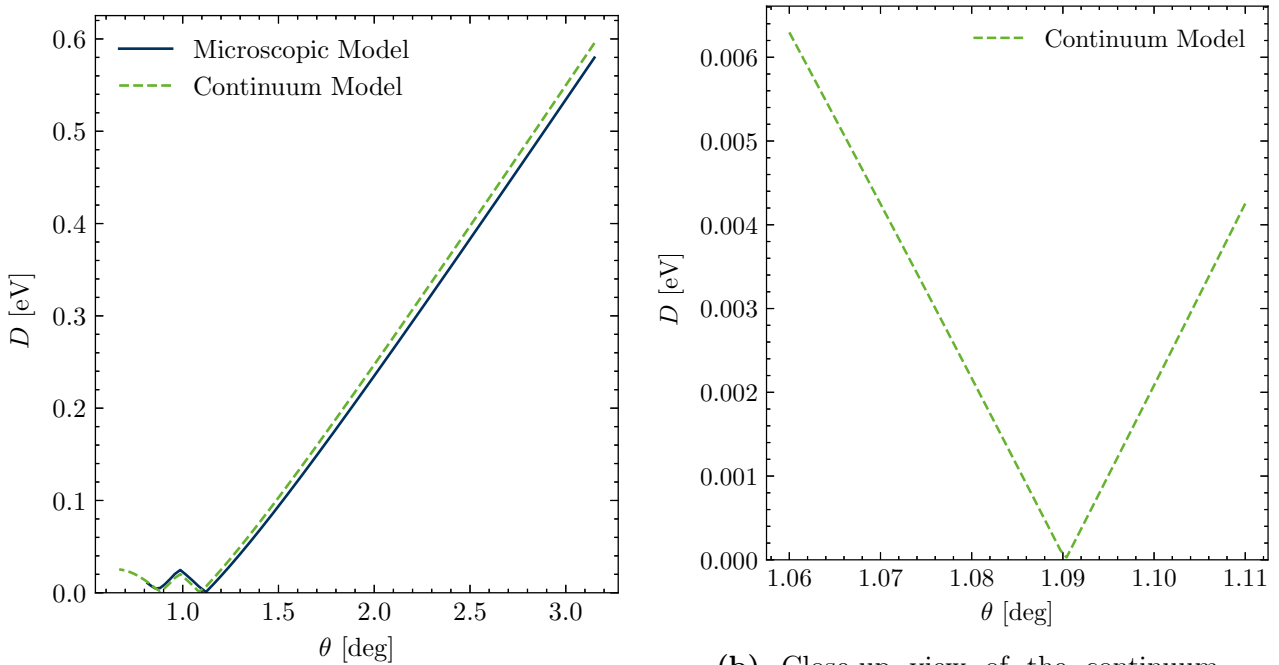


**Figure 2.13:** Interlayer coupling strength  $V_{pp\sigma}$  that minimizes the Fermi velocity at a given twist angle in the microscopic model. Results are shown both for a constant interlayer spacing and in the presence of corrugation effects. The reference value of  $V_{pp\sigma}^0 = 0.48$  eV given in Section 2.3 should yield the most realistic results.



(a) Comparison of band separations for both models.

(b) Close-up view of the continuum model band separation in the vicinity of the minimum separation.

**Figure 2.14:** Energy separation of the flat valence and conduction bands at the  $\Gamma$  point.



We conclude this section by remarking on the sensitivity of the results to the choice of cutoff thresholds Eqs. (2.19) and (2.26): When choosing the cutoff of  $4a_0$  suggested in Ref. [16] for the microscopic Hamiltonian, one observes oscillations in the Fermi velocity and band separation at small twist angles, instead of the smooth behaviour present at a cutoff of  $6a_0$ . Similar behaviour occurs with the continuum approximation. This may be the case because on an intuitive level, a reduction of the twist angle corresponds to zooming in on the band structure due to Brillouin zone folding. Thus, at lower twist angles, slight changes to the energy bands due to higher order processes become more relevant.



# 3 Interactions

## 3.1 Mean-field approximation

An important feature of the non-interacting tight binding Hamiltonian Eq. (2.14) is that the fermionic operators always occur as bilinear terms, meaning that the Hamiltonian is a sum of single particle observables [10]: For an operator of this type, one readily obtains the Bloch matrix by Fourier transforming the Hamiltonian, and the problem of finding energy bands reduces to a matrix eigenvalue problem. This effective single particle treatment is generally not possible for a Hamiltonian that includes interaction terms coupling two or more fermions. Given an operator of this type, we may instead obtain an effective single particle description with the help of the mean-field approximation [10]: Specifically, given a product of fermionic number operators  $n_\alpha n_\beta = c_\alpha^\dagger c_\alpha c_\beta^\dagger c_\beta$ , the idea is to express the operators as  $n_\alpha = \langle n_\alpha \rangle + \delta n_\alpha$ , where  $\langle n_\alpha \rangle$  is the ensemble average of  $n_\alpha$ , and the operator  $\delta n_\alpha$  represents fluctuation around the mean value. One thus obtains

$$\begin{aligned} n_\alpha n_\beta &= \langle n_\alpha \rangle \langle n_\beta \rangle + \langle n_\alpha \rangle \delta n_\beta + \langle n_\beta \rangle \delta n_\alpha + \delta n_\alpha \delta n_\beta \\ &= \langle n_\alpha \rangle \langle n_\beta \rangle + \langle n_\alpha \rangle (n_\beta - \langle n_\beta \rangle) + \langle n_\beta \rangle (n_\alpha - \langle n_\alpha \rangle) + \delta n_\alpha \delta n_\beta \\ &\approx \langle n_\alpha \rangle n_\beta + \langle n_\beta \rangle n_\alpha - \langle n_\alpha \rangle \langle n_\beta \rangle, \end{aligned}$$

where in the final line, we have assumed the product of the fluctuations to be negligibly small. We may additionally write  $n_\alpha n_\beta = -(c_\alpha^\dagger c_\beta)(c_\beta^\dagger c_\alpha)$ , and by a similar argument as above obtain

$$n_\alpha n_\beta \approx - \left( \langle c_\alpha^\dagger c_\beta \rangle c_\beta^\dagger c_\alpha + \langle c_\beta^\dagger c_\alpha \rangle c_\alpha^\dagger c_\beta - \langle c_\alpha^\dagger c_\beta \rangle \langle c_\beta^\dagger c_\alpha \rangle \right).$$

For general products of operator, a more rigorous derivation of possible decoupling channels is obtained by Wick's theorem [10, 11].

The two substitutions of interest

$$n_\alpha n_\beta \rightarrow \langle n_\beta \rangle n_\alpha + \langle n_\alpha \rangle n_\beta - \langle n_\alpha \rangle \langle n_\beta \rangle, \quad (3.1)$$

$$n_\alpha n_\beta \rightarrow -\Delta_{\alpha\beta} c_\alpha^\dagger c_\beta - \Delta_{\beta\alpha} c_\beta^\dagger c_\alpha + \Delta_{\alpha\beta} \Delta_{\beta\alpha}, \quad (3.2)$$

with  $\Delta_{\alpha\beta} = \langle c_\beta^\dagger c_\alpha \rangle = \Delta_{\beta\alpha}^*$ , are known as the onsite and bond decoupling channels, respectively. For each lattice site and each bond in the lattice, the above decoupling introduces one unknown

parameter into the Hamiltonian. In general, the effective energy bands are then obtained by choosing the parameters such that the free energy of the system is minimized, i.e. we solve the optimization problem [29]

$$F = -\frac{1}{\beta} \sum_n \sum_{\mathbf{k}} \ln(1 + e^{\beta \varepsilon_n(\mathbf{k})}) \rightarrow \min. \quad (3.3)$$

Here,  $\beta = 1/k_B T$ ,  $\sum_n$  is taken over the energy bands of the system, and  $\sum_{\mathbf{k}}$  ranges over the allowed momenta. For computational convenience, the latter are usually determined by imposing periodic boundary conditions for the system, giving [11]

$$\mathbf{k} = \frac{m_1}{M_1} \mathbf{b}_1 + \frac{m_2}{M_2} \mathbf{b}_2,$$

with  $M_l$  the total number of lattice sites along direction  $l$  and  $0 \leq m_l < M_l$ . If one is interested only in the case of  $T = 0$ , the free energy  $F = U - TS$  reduces to the internal energy

$$U = \sum_{n \text{ occ.}} \sum_{\mathbf{k}} \varepsilon_n(\mathbf{k}),$$

where  $\sum_{n \text{ occ.}}$  is now taken over the occupied bands of the system.

To bring the optimization problem Eq. (3.3) within reach of the available computational tools, one may choose a periodic ansatz for the mean-field parameters that represents a correlated phases of interest. For instance, Raghu et al. [30] show that monolayer graphene can sustain a charge density wave state, where the mean-field parameters  $\langle n_A \rangle$ ,  $\langle n_B \rangle$  for all A and B sites are chosen according to

$$\begin{aligned} \frac{1}{2} (\langle n_A \rangle - \langle n_B \rangle) &= \rho, \\ \langle n_A \rangle + \langle n_B \rangle &= \text{const.}, \end{aligned}$$

with the former equation describing the mismatch in charge between A and B sites, and the latter equation guaranteeing conservation of charge. Specifically, we may choose  $\langle n_A \rangle + \langle n_B \rangle = 0$ , since the value of  $\langle n_A \rangle + \langle n_B \rangle$  is the same for both phases and only results in a constant energy shift. If only the charge density wave state is considered, a single mean-field parameter  $\rho$  then remains to be determined. When the optimization problem yields a value of  $\rho \neq 0$ , sublattice symmetry is broken and the system enters a gapped phase, which indeed replaces the usual semimetallic state of graphene in some portions of the phase diagram [29, 30].

Besides the charge density wave state, one can also locate a Kekulé phase and a quantum anomalous Hall (QAH) state in the phase diagram of monolayer graphene [29, 30]. The former is characterized by distorted nearest neighbour bonds, whereas the latter exhibits circulating currents between next-to-nearest neighbour sites.

Instead of assuming some ansatz for potential correlated phases, one can also solve directly for approximate Slater determinant wave functions of the system with the help of the Hartree-Fock approximation [10, 11]. This involves iteratively solving the non-linear Hartree-Fock equation, and thus causes a considerable computational expense [11]. A number of studies [6–8, 31] have applied this framework to TBG. Most notably, Bultinck et al. [7] find the insulating *Kramers intervalley-coherent* (KIVC) state, characterized by circulating nearest neighbour currents, to be the ground state of magic angle TBG at charge neutrality in a continuum description. The continuum model phase diagram for all possible integer fillings of the flat bands has been mapped out by Kwan and coworkers [8]. Sánchez and Stauber [31] observe a competition between the KIVC and a spin polarized state at charge neutrality for a microscopic Hamiltonian, though with a different interaction term than the one we use below.

## 3.2 Electron-electron interactions in the microscopic model

To account for the effects of electron-electron interactions in TBG on a microscopic level, we augment the tight binding Hamiltonian  $\mathcal{H}_0$  in Eq. (2.15) by an interaction term  $\mathcal{H}_I$  [32], with

$$\mathcal{H}_I = \underbrace{U_{00} \sum_i n_{i\uparrow} n_{i\downarrow}}_{=\mathcal{H}_{I,0}} + \frac{1}{2} \underbrace{\sum_{\substack{i \neq j \\ \sigma, \sigma'}} U(\mathbf{R}_i - \mathbf{R}_j) n_{i\sigma} n_{j\sigma'}}_{=\mathcal{H}_{I,1}}, \quad (3.4)$$

and the fermionic number operators  $n_{i\sigma} = c_{i\sigma}^\dagger c_{i\sigma}$ . The resulting operator  $\mathcal{H} = \mathcal{H}_0 + \mathcal{H}_I$  is known as the generalized Hubbard Hamiltonian. Evidently, it is no longer quadratic in the fermionic operators and hence cannot be diagonalized using only a Fourier transform. Instead, we will turn to the mean-field approximation to obtain a useful description of the system that can accommodate the strongly correlated phases of TBG. For brevity, we will focus on the mean-field decoupling for the term  $\mathcal{H}_{I,1}$ , and only state the final result for  $\mathcal{H}_{I,0}$ . In addition,

Interaction Parameter	Value [eV]
$U_{00}$	9.3
$U_{01}$	5.5
$U_{02}$	4.1
$U_{03}$	3.6

**Table 3.1:** Effective strength of Coulomb interactions in freestanding graphene as calculated by Wehling et al. [32]. The parameters  $U_{01}$ ,  $U_{02}$ , ... correspond to the values of  $U(\mathbf{R})$  in Eq. (3.4) for nearest neighbour terms, next-to-nearest neighbour terms, etc. The effects of electrons outside of  $\pi$  bonds are taken into account based on the constrained random phase approximation.

as long as we do not assume the existence of any kind of charge density wave state, it suffices to consider the bond decoupling channel, as the onsite decoupling only contributes a constant energy offset to all states.

Using the notation of Eq. (2.15), the interaction term  $\mathcal{H}_{I,1}$  can be expressed as

$$\mathcal{H}_{I,1} = \frac{1}{2} \sum_{\mathbf{L}, \mathbf{L}'} \sum_{\substack{X, X' \\ \sigma, \sigma'}} U((\mathbf{R}_X + \mathbf{L}) - (\mathbf{R}_{X'} + \mathbf{L}')) n_{\sigma}(\mathbf{R}_X + \mathbf{L}) n_{\sigma'}(\mathbf{R}_{X'} + \mathbf{L}'),$$

where we have defined  $U(\mathbf{0}) = 0$ , such that onsite terms do not need to be excluded from the sum explicitly. Inserting the bond decoupling Eq. (3.2), one obtains

$$\begin{aligned} \mathcal{H}_{I,1} &= \frac{1}{2} \underbrace{\sum_{\mathbf{L}, \mathbf{L}'} \sum_{\substack{X, X' \\ \sigma, \sigma'}} U((\mathbf{R}_X + \mathbf{L}) - (\mathbf{R}_{X'} + \mathbf{L}')) |\Delta_{X\sigma, X'\sigma'}|^2}_{=: E_{I,1}^0} \\ &\quad - \frac{1}{2} \sum_{\mathbf{L}, \mathbf{L}'} \sum_{\substack{X, X' \\ \sigma, \sigma'}} U((\mathbf{R}_X + \mathbf{L}) - (\mathbf{R}_{X'} + \mathbf{L}')) \left( \Delta_{X\sigma, X'\sigma'} c_{X\sigma}^{\dagger}(\mathbf{R}_X + \mathbf{L}) c_{X'\sigma'}(\mathbf{R}_{X'} + \mathbf{L}') + \text{h.c.} \right). \end{aligned}$$

The contribution  $E_{I,1}^0$  leaves the energy levels unaffected, but must be taken into account when computing the free energy Eq. (3.3). Fourier transforming the fermionic operators, we then arrive at

$$\begin{aligned} \mathcal{H}_{I,1} &= E_{I,1}^0 - \frac{1}{2} \sum_{\mathbf{L}, \mathbf{L}'} \sum_{\substack{X, X' \\ \sigma, \sigma'}} U((\mathbf{R}_X + \mathbf{L}) - (\mathbf{R}_{X'} + \mathbf{L}')) \\ &\quad \times \frac{1}{N_M} \sum_{\mathbf{k}, \mathbf{k}'} \left( \Delta_{X\sigma, X'\sigma'} e^{i\mathbf{k} \cdot (\mathbf{R}_X + \mathbf{L})} e^{-i\mathbf{k}' \cdot (\mathbf{R}_{X'} + \mathbf{L}')} c_{X\sigma}^{\dagger}(\mathbf{k}) c_{X'\sigma'}(\mathbf{k}') + \text{h.c.} \right), \end{aligned}$$

with  $N_M$  denoting the number of moiré unit cells in the lattice. If we define  $\Delta\mathbf{L} = \mathbf{L}' - \mathbf{L}$  and substitute  $\sum_{\mathbf{L}, \mathbf{L}'} \rightarrow \sum_{\mathbf{L}, \Delta\mathbf{L}}$ , the sum over  $\mathbf{L}$  can be executed, and since  $\sum_{\mathbf{L}} e^{-i(\mathbf{k} - \mathbf{k}') \cdot \mathbf{L}} = N_M \delta_{\mathbf{k}\mathbf{k}'}$ , we find

$$= E_{I,1}^0 - \frac{1}{2} \sum_{\Delta\mathbf{L}} \sum_{\substack{X, X' \\ \sigma, \sigma'}} \sum_{\mathbf{k}} U(\mathbf{R}_X - \mathbf{R}_{X'} + \Delta\mathbf{L}) \left( \Delta_{X\sigma, X'\sigma'} e^{i\mathbf{k} \cdot (\mathbf{R}_X - \mathbf{R}_{X'} + \Delta\mathbf{L})} c_{X\sigma}^{\dagger}(\mathbf{k}) c_{X'\sigma'}(\mathbf{k}) + \text{h.c.} \right).$$

This result can be expressed as

$$\mathcal{H}_{I,1} = E_{I,1}^0 + \sum_{\mathbf{k}} \Psi_{\mathbf{k}}^{\dagger} h_{I,1}(\mathbf{k}) \Psi_{\mathbf{k}},$$

where  $h_{I,1}(\mathbf{k})$  is the contribution to the systems Bloch Hamiltonian, with matrix elements

$$\begin{aligned}
h_{I,1}^{X\sigma,X'\sigma'}(\mathbf{k}) &= -\frac{1}{2} \sum_{\Delta\mathbf{L}} U(\mathbf{R}_X - \mathbf{R}_{X'} + \Delta\mathbf{L}) e^{i\mathbf{k}\cdot(\mathbf{R}_X - \mathbf{R}_{X'} + \Delta\mathbf{L})} \Delta_{X\sigma,X'\sigma'} \\
&\quad - \frac{1}{2} \sum_{\Delta\mathbf{L}} U(\mathbf{R}_{X'} - \mathbf{R}_X + \Delta\mathbf{L}) e^{i\mathbf{k}\cdot(\mathbf{R}_{X'} - \mathbf{R}_X + \Delta\mathbf{L})} \Delta_{X'\sigma',X\sigma} \\
&= - \sum_{\Delta\mathbf{L}} U(\mathbf{R}_X - \mathbf{R}_{X'} + \Delta\mathbf{L}) e^{i\mathbf{k}\cdot(\mathbf{R}_X - \mathbf{R}_{X'} + \Delta\mathbf{L})} \Delta_{X\sigma,X'\sigma'}.
\end{aligned} \tag{3.5}$$

Here, the final equality was obtained by taking  $\Delta\mathbf{L} \rightarrow -\Delta\mathbf{L}$  in the second sum and exploiting that  $U(\mathbf{R}) = U(-\mathbf{R})$  and  $\Delta_{\alpha\beta} = \Delta_{\beta\alpha}^*$ .

An analogous calculation for  $\mathcal{H}_{I,0}$  yields the contributions

$$h_{I,0}^{X\sigma,X'\sigma'}(\mathbf{k}) = -U_{00} (\delta_{XX'} \delta_{\sigma\uparrow} \delta_{\sigma'\downarrow} \Delta_{X\uparrow,X\downarrow} + \delta_{XX'} \delta_{\sigma\downarrow} \delta_{\sigma'\uparrow} \Delta_{X\downarrow,X\uparrow})$$

and

$$E_{I,0}^0 = U_{00} N_M \sum_X |\Delta_{X\uparrow,X\downarrow}|^2,$$

for the onsite term.

Values for the effective interaction strength  $U$  up to third nearest neighbour sites have been determined by Wehling et al. [32] based on first principles calculations, and are summarized in Table 3.1. Screening effects due to the remaining electrons that are not participating in  $\pi$  bonds are taken into account based on the *constrained random phase approximation*. Wehling et al. additionally point out that the ratio of interaction strength and hopping amplitude is sensitive to strain in the graphene sheet. Further, the effective interaction strengths in Table 3.1 apply to freestanding graphene with a dielectric constant of  $\varepsilon \approx 2.5$ <sup>1</sup> [32]. To adapt the description to experimental conditions, screening effects due to metallic gates need to be taken into account, increasing the dielectric constant and scaling the interaction potential according to  $U \sim 1/\varepsilon$  [7]. As a rough estimate, we choose a value of  $\varepsilon = 9.5$  to match the range of values  $\varepsilon = 7 - 12$  considered by Bultinck et al. [7], meaning that the values in Table 3.1 are scaled by a factor of  $(9.5/2.5)^{-1}$ .

---

<sup>1</sup>Wehling et al. [32] actually report a value  $\varepsilon \approx 2.4$ , but a value of  $\varepsilon \approx 2.5$  was erroneously used in our mean-field calculations. Since this only affects rough estimates for reference values of the interaction strength, we continue to assume a value of  $\varepsilon \approx 2.5$  in the remainder of the text.

### 3.3 Current operator for the generalized Hubbard Hamiltonian

A number of correlated state of matter in TBG are characterized by circulating currents between lattice sites, and an understanding of the current operator for the generalized Hubbard Hamiltonian is thus a prerequisite for the parametrization of such states. In analogy with classical electromagnetism, we assume the integrated probability current from site  $j$  to all other lattice sites satisfies  $J_j = -\partial_t n_j$ , with  $n_j = c_j^\dagger c_j$  the number of electrons at site  $j$ . Switching to the Heisenberg picture, we can compute

$$\begin{aligned} \partial_t n_j &= \frac{i}{\hbar} [\mathcal{H}, n_j] \\ &= \frac{i}{\hbar} [\mathcal{H}_0, n_j] && (\mathcal{H}_I \text{ only contains number operators}) \\ &= \frac{i}{\hbar} \sum_{i \neq k} t(\mathbf{R}_i - \mathbf{R}_k) [c_i^\dagger c_k, n_j] \\ &= \frac{i}{\hbar} \sum_i \left( t(\mathbf{R}_i - \mathbf{R}_j) c_i^\dagger c_j - \text{h.c.} \right). \end{aligned}$$

Here, we have exploited that  $[c_i^\dagger, n_j] = -\delta_{ij} c_j^\dagger$ , and thus

$$\begin{aligned} [c_i^\dagger c_k, n_j] &= c_i^\dagger [c_k, n_j] + [c_i^\dagger, n_j] c_k \\ &= \delta_{kj} c_i^\dagger c_j - \delta_{ij} c_j^\dagger c_k. \end{aligned}$$

The current from site  $j$  to some specific lattice site  $i$  can then be interpreted to be

$$\begin{aligned} \langle J_{ji} \rangle &= -\frac{i}{\hbar} \left( t(\mathbf{R}_i - \mathbf{R}_j) \langle c_i^\dagger c_j \rangle - \text{h.c.} \right) \\ &= \frac{2}{\hbar} t(\mathbf{R}_i - \mathbf{R}_j) \text{Im}(\Delta_{ji}), \end{aligned} \tag{3.6}$$

where we have exploited that  $t(\mathbf{R}) = t(-\mathbf{R})$  and  $\langle c_i^\dagger c_j \rangle = \Delta_{ji}$  is a mean-field parameter.

A similar result for the probability current on a lattice, though with a derivation in the language of first quantization, is given in Ref. [33].

### 3.4 Candidate ground states

The phase diagram of TBG contains a rich variety of states of matter, and a systematic study of all potential ground states can be carried out using the previously mentioned Hartree-Fock approximation [7, 31]. Here, we instead restrict ourselves to the parametrization of two particular phases of interest, namely the KIVC state and a QAH phase.



State of Matter	$C_2$	$\mathcal{T}$	$C_2\mathcal{T}$	$U_V(1)$
Semimetallic (SM)	✓	✓	✓	✓
Valley-Hall (VH)	✗	✓	✗	✓
Quantum Anomalous Hall (QAH)	✓	✗	✗	✓
Valley-Polarized (VP)	✗	✗	✓	✓
Kramers Intervalley-Coherent (KIVC)	✗	✗	✗	✗

**Table 3.2:** Candidate ground states and their symmetries in magic angle TBG as reported by Bultinck et al. [7].

In total, Bultinck et al. [7] report five different groups of candidate ground states for magic angle TBG at charge neutrality, all of which are listed in Table 3.2. Different phases are distinguished by the symmetries of the Hamiltonian that are being preserved, the symmetries of interest to us being twofold rotational symmetry  $C_2$ , time reversal symmetry  $\mathcal{T}$ , and valley charge conservation  $U_V(1)$ . The latter is only an approximate symmetry in a microscopic framework. We will return to the issue of valley polarization below.

Although Table 3.2 lists five candidate states, it should be sufficient to consider only four phases when mapping out the phase diagram, since the free energies of the VH and QAH states coincide for the continuum Hamiltonian [7]. We choose to focus on the QAH state, since there exists a simple parametrization with the desired symmetries.

When choosing an ansatz for the mean-field parameters, both real and imaginary parts need to be parametrized. The former simply yield a renormalization of the hopping amplitudes according to Eq. (3.5). This can cause the emergence of gapped phases such as the Kekulé phase in monolayer graphene [29] if the  $C_2$  symmetry of the Hamiltonian is broken, but it will not cause time reversal symmetry breaking. On the other hand, the imaginary part of a mean-field parameter leads to a non-vanishing imaginary part in the renormalized hopping amplitude, and is thus always associated with broken  $\mathcal{T}$ . Intuitively, this is sensible because the imaginary part causes a current between lattice sites according to Eq. (3.6).

We denote the real part of the nearest neighbour hopping renormalization for all candidate ground states as  $\delta t$ . Values of  $\delta t$  are assumed to be the same for all lattice sites, as this is sufficient for a parametrization of ground states with the desired symmetries. Higher order renormalizations are neglected since during preliminary mean-field calculations, these parameters always converged to negligible values. Generally, one would also need to consider an onsite renormalization, but we focus on spinless fermions below. Following Weeks and Franz [29], we additionally assume that  $\delta t$  takes on a fixed value of  $\delta t = 0.262$  throughout the phase diagram. This limits the computational expense by reducing the number of mean-field parameters, and preliminary calculations show that the actual value only varies slightly around 0.262.

For the parametrization of imaginary parts, it turns out that nearest and next-to-nearest neighbour currents are sufficient to produce states with the desired symmetry properties:

- The KIVC state is characterized by the circulating current pattern shown in Fig. 3.1.

Current Pattern	$C_2$	$C_2\mathcal{T}$	$U_V(1)$	State of Matter
(+ + + +)	✓	✗		(Net Magnetization)
(+ + + -)	✗	✗		(Net Magnetization)
(+ + - -)	✓	✗	✓	QAH
(+ - + -)	✗	✓	✓	VP
(+ - - +)	✗	✓	✓	VP

**Table 3.3:** Possible next-to-nearest neighbour current configuration in a graphene bilayer. Current configurations are denoted as tuples (A1, B1, A2, B2), where each component denotes the orientation (clockwise or counter-clockwise) of the current loop in the respective sublattice. Only configurations that are not related by any symmetry operation are shown. We additionally list the symmetries of each configuration, as well as the corresponding phase according to Table 3.2.  $U_V(1)$  symmetry breaking is assessed using the valley polarization operator Eq. (3.7). States with a net magnetization are not considered further.

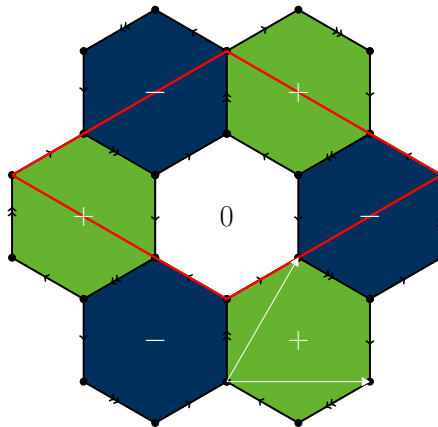


**Figure 3.1:** Circulating nearest neighbour currents of the KIVC phase [7]. The enlarged unit cell of this  $\sqrt{3} \times \sqrt{3}$  order is highlighted in red, and the original monolayer lattice vectors are shown in white. The colour of a plaquette denotes the direction of its magnetization density.

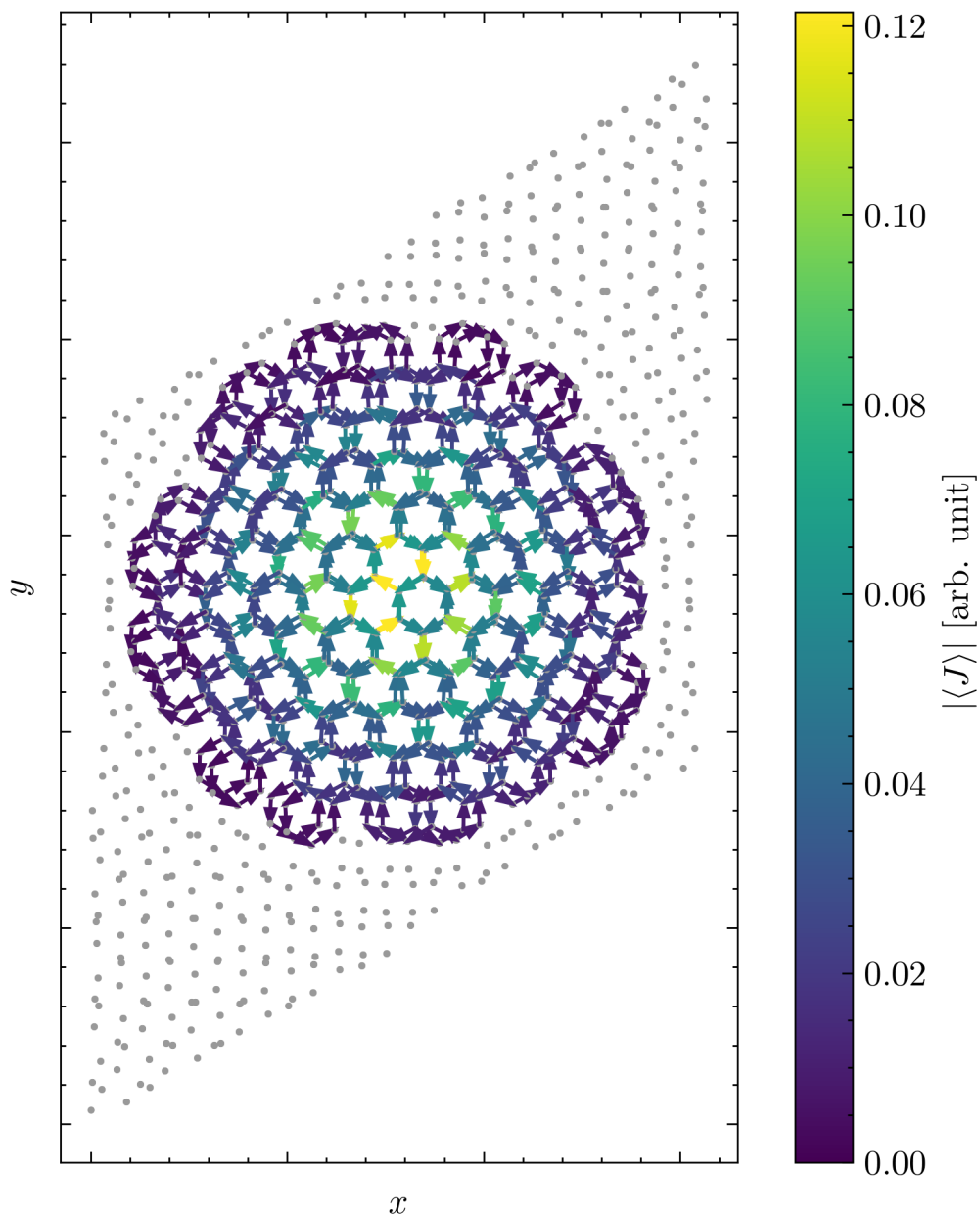


**Figure 3.2:** TBG unit cell with the spatially modulated current pattern of the KIVC phase. The dimensionless modulation  $m$  is defined as  $m(\mathbf{r}) = \max(0, 1 - |\mathbf{c} - \mathbf{r}|/(R - a))$ , where  $\mathbf{c}$  is the center of the unit cell,  $R$  is the radius of its inscribed circle, and the lattice constant  $a$  is subtracted to ensure there are no currents across unit cell bounds. The current around a given plaquette is determined by evaluating the modulation function at the center of the plaquette. If a link is adjacent to two plaquettes with nonzero magnetization, the currents of both plaquettes are added together in the link, leading to some particularly bright spots in the visualization. The disk of nonzero current appears to contain “gaps” at its boundary, corresponding to the plaquettes with zero magnetization in Fig. 3.1.

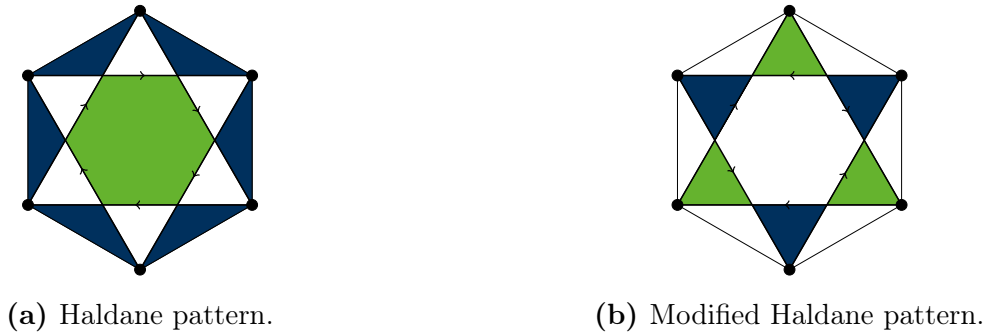


**Figure 3.3:** Next-to-nearest neighbour current loops in monolayer graphene. The color of a segment indicates its magnetization density. These figures have been adapted from Ref. [34].

This can be considered a  $\sqrt{3} \times \sqrt{3}$  order, since the primitive lattice vectors of each monolayer are enlarged by a factor of  $\sqrt{3}$ . The lattice vectors are additionally rotated by  $30^\circ$  with respect to the original monolayer lattice vectors, and as a consequence of this rotation, the current pattern is incommensurate with the TBG unit cell. This issue can be circumvented by spatially modulating the current such that all currents across unit cell boundaries vanish, and the TBG unit cell is left unchanged. A spatial modulation is indeed present in the Hartree-Fock results of Bultinck et al., but the details of this modulation are unclear. As illustrated in Fig. 3.2, we assume a simple linear decrease in intensity as the distance to the AA stacking region of the unit cell increases.

- Up to symmetry, the honeycomb lattice can support two next-to-nearest neighbour current configurations [34], commonly termed the Haldane and modified Haldane pattern, and depicted in Fig. 3.3a and Fig. 3.3b, respectively. For a bilayer, one finds a total of  $2^4 = 16$  current configurations by considering all possible combinations of clockwise and counter-clockwise currents in the A1, B1, A2 and B2 sublattices. However, most of these configurations are related to one another by  $\mathcal{T}$ ,  $C_2$  or an exchange of layers, and thus yield identical free energies. Hence, only five distinct groups of configurations need to be considered, all of which are listed in Table 3.3, describing both a VP and QAH phase. Here, there is no need to assume a spatially modulated current.

Based on the above considerations, we are left with the SM and KIVC states, a QAH phase, and two possible configurations for a VP phase. However, we choose to neglect the VP state for all mean-field calculations, since in some preliminary computations at isolated points in the phase diagram, neither configuration was found to be energetically favourable over the SM state. Naturally, this does not rule out the possibility of a VP state for the Hubbard Hamiltonian, and in particular, allowing for spatial modulations or additional currents could stabilize this phase.

We have already alluded to the fact that a distinguishing feature of the KIVC phase is its lack of valley polarization. While a definite valley polarization for all energy eigenstates is

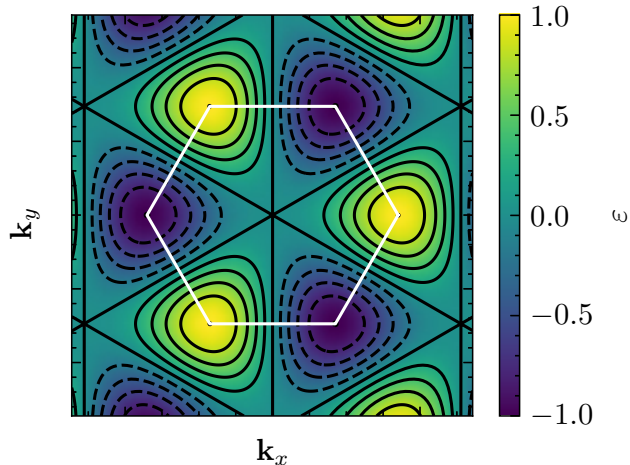


**Figure 3.4:** Eigenvalues  $\varepsilon$  of the valley polarization operator Eq. (3.7) for a graphene monolayer. The first Brillouin zone is highlighted in white. Dashed contour lines correspond to negative eigenvalues.

inherent to the (non-interacting) continuum description, there is no obvious definition of this quantity in a microscopic model, since in this framework, valley charge conservation is merely an emergent symmetry at small twist angles [35]. Nonetheless, Ramires and Lado [35] manage to introduce a valley polarization operator  $V_\ell$  that allows one to distinguish contributions from either of the two valleys of layer  $\ell$ . The key idea is to find a minimal tight binding Hamiltonian for graphene for which the two valleys correspond to different eigenenergies, and thus become distinguishable. In a slightly twisted graphene bilayer, the  $\mathbf{K}$  points ( $\mathbf{K}'$  points) of both monolayers  $\ell$  are positioned almost on top of one another. The interlayer coupling then hybridizes states from the overlapping valleys [15], and the bilayer valley polarization  $V$  can thus be determined by summing the contributions from both layers, i.e.  $V = V_1 + V_2$ .

A minimal Hamiltonian  $V_\ell$  for monolayer graphene that yields distinct eigenenergies for both valleys is obtained by setting all real valued hopping terms to zero, and choosing imaginary hoppings corresponding to the Haldane pattern Fig. 3.3a [35]. In second quantization,  $V_\ell$  can then be expressed as

$$V_\ell = \frac{i}{3\sqrt{3}} \sum_{\langle\langle i,j \rangle\rangle \in \ell} \eta_{ij} \sigma_z^{ij} c_i^\dagger c_j, \quad (3.7)$$

where  $\eta_{ij} = \pm 1$  for clockwise (counter-clockwise) hopping, and the prefactor normalizes the eigenvalues to a range of  $[-1, 1]$ . The spectrum of  $V_\ell$  is illustrated in Fig. 3.4.

With the help of the operator  $V$ , we can assign a valley polarization  $\langle V \rangle$  to each eigenstate in a given band, and use the results to classify a phase of matter as valley polarized or intervalley-coherent. Expectation values of the valley polarization operator for the phases under consideration are shown in Fig. 3.5, and indicate that only the KIVC breaks the approximate  $U_V(1)$  symmetry of the Hamiltonian. Here, we assume that  $U_V(1)$  breaking is independent of the

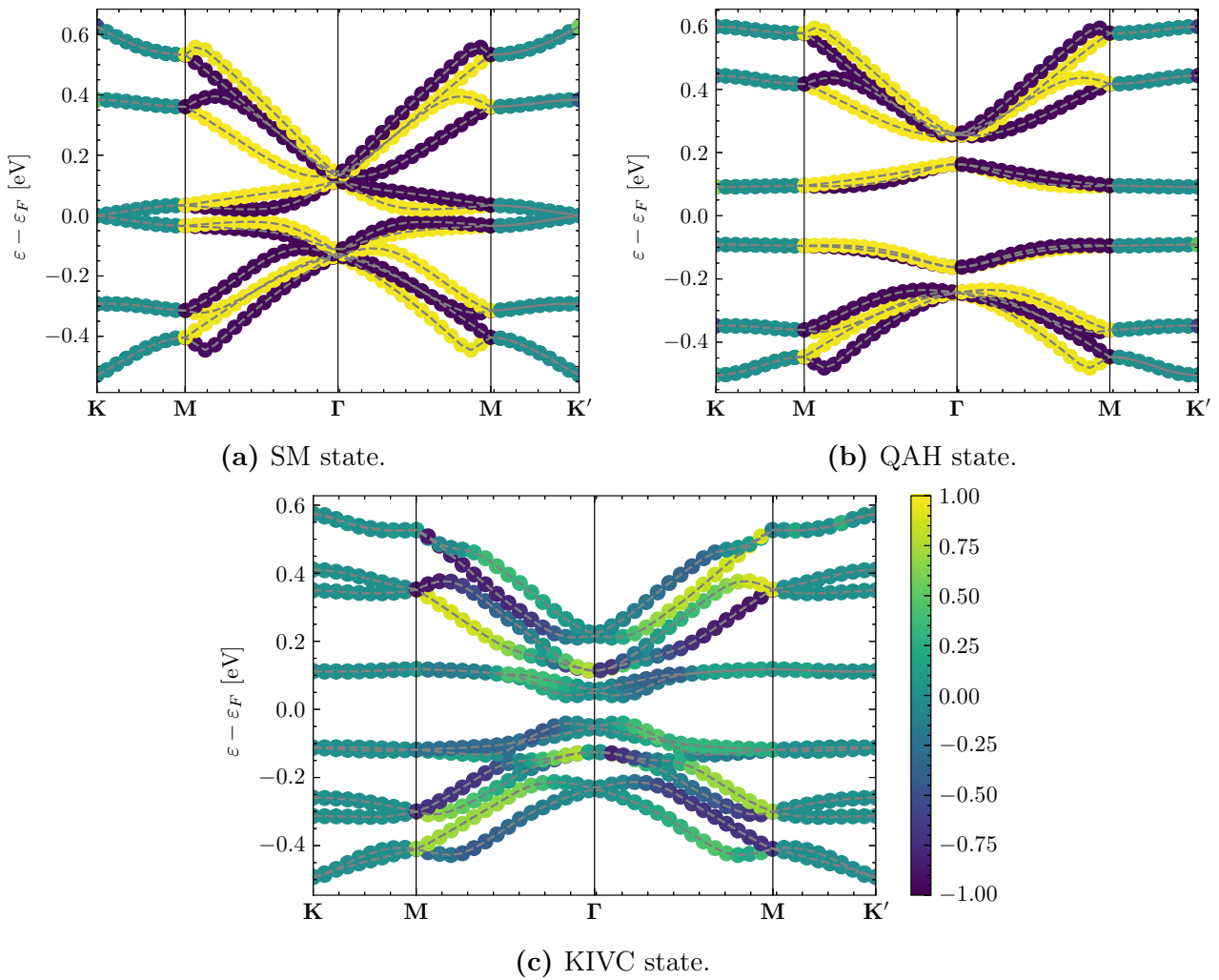


**Figure 3.5:** Band structure and valley polarization in the three phases under consideration. Note how the calculated valley polarization becomes invalid in the presence of degeneracies due to the ambiguity in choosing eigenvectors from the degenerate subspace. These illustrations were generated by assuming arbitrary small values for the respective order parameters, i.e. they do not represent the result of an actual mean-field calculation.

precise parameters of the model, and the classification of a phase remains unchanged at all sufficiently small twist angles. Fig. 3.5 further illustrates how time reversal symmetry breaking causes the emergence of gapped phases. On a qualitative level, the KIVC bands in Fig. 3.5c are in good agreement with the results of Bultinck et al.

### 3.5 Quantum phase diagrams

In the following, we map out the phase diagram of our Hamiltonian for different slices of its parameter space by solving the optimization problem Eq. (3.3).

We consider the SM, KIVC and QAH states introduced in the previous section and neglect interaction terms beyond the next-to-nearest neighbour level. We additionally restrict ourselves to the case of charge neutrality at zero temperature, and consider only spinless fermions. In total, this leaves us with a four-dimensional parameter space: Besides the twist angle, we can also adjust the interaction strengths  $U_{01}$  and  $U_{02}$  in Table 3.1. In addition, it is helpful to consider different interlayer coupling strengths  $V_{pp\sigma}$ , since this impacts the location of the magic angle (see Fig. 2.13). One can thus adjust  $V_{pp\sigma}$  in order to study magic angle TBG at relatively large twist angles where mean-field computations are not prohibitively expensive. Because the magic angle changes approximately linearly with  $V_{pp\sigma}$ , it is even possible to define an effective twist angle [7]  $\tilde{\theta} = \theta V_{pp\sigma}^0 / V_{pp\sigma}$  for this *distorted* model at an angle  $\theta$ . However, an effective twist angle and its undistorted counterpart may correspond to unit cells of vastly different sizes, and it is certainly possible that this causes differences in the physical behaviour. To compute the free energy Eq. (3.3), it is additionally important to determine all occupied eigenenergies of the Hamiltonian. Since the sparse diagonalization algorithm mentioned in Section 2.3 is most suitable for determining a small subset of eigenvalues, we now switch to a full diagonalization of the Bloch Hamiltonian by means of *Python's NumPy* library. Finally, we assume a constant interlayer spacing of  $d = 0.335$  nm and neglect corrugation effects in the remainder of this section, leading to an increase in the magic angle.

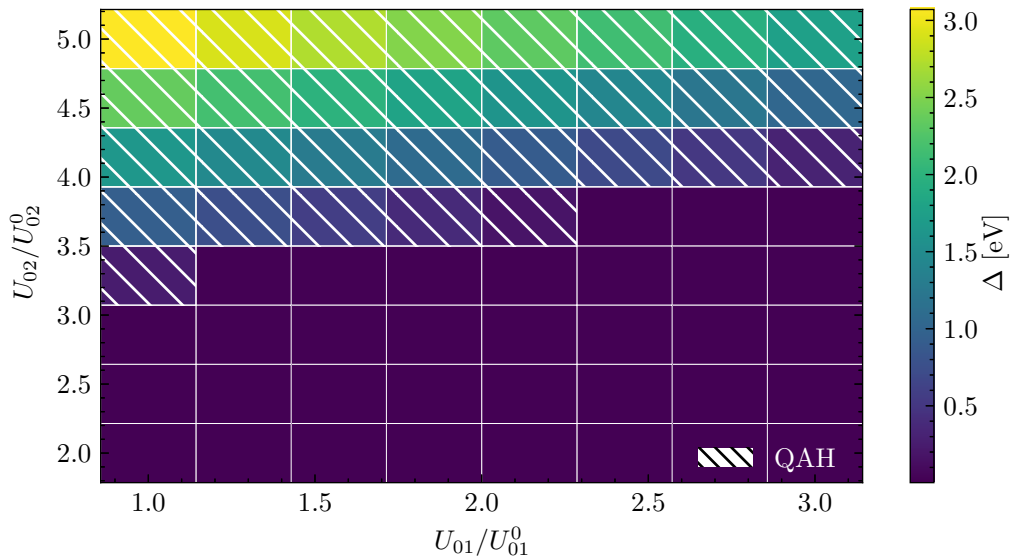
The order parameters of the KIVC and QAH phase are chosen to linearly scale the magnitude of the respective currents. Results of the mean-field computation on a  $5 \times 5$  grid in  $k$ -space are shown in Fig. 3.6. The QAH order parameter was found to be irresponsive to changes in the twist angle, and we instead show a slice in  $U_{01}$ - $U_{02}$ -space in Fig. 3.6a. In the parameter regime under consideration, the QAH phase only stabilizes at relatively large interaction strengths  $U_{02} \gtrsim 3U_{02}^0$ , and an increase in the nearest neighbour interaction  $U_{01}$  weakens the QAH order. The KIVC on the other hand reacts sensitively to changes in the twist angle, and in particular, it appears that finite KIVC order manifests only when approaching the magic angle. Whether the KIVC continues to be energetically favourable for a wide range of angles below the magic angle is unclear.

The phase transition from SM to KIVC order at  $U_{01} = U_{01}^0$  is shown in more detail in Fig. 3.7.

It is not clear whether the transition is of first or second order, i.e. whether the order parameter evolves continuously at the critical effective twist angle. However, we have confirmed that if the transition is of first order, the discontinuity has a height of less than 0.001.

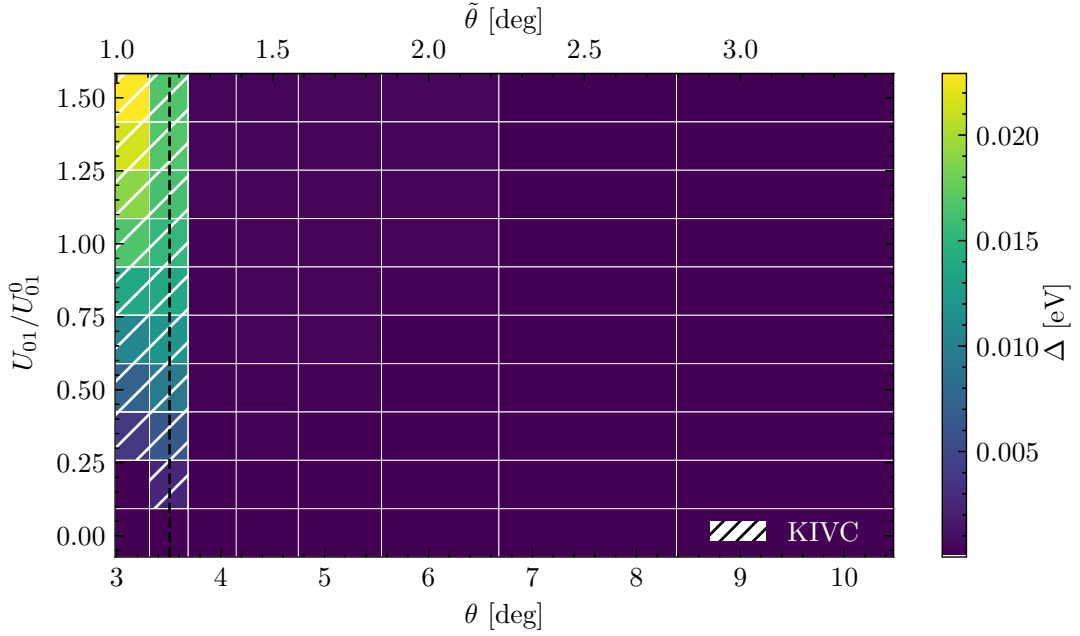
At the  $\mathbf{K}$  point, the KIVC gap for the magic angle, with  $U_{01} = U_{01}^0$ , is roughly 15 meV. Despite the simplicity of our model, this is only somewhat lower than the value of roughly 50 meV obtained by Bultinck et al. [7]. In the parameter regime under consideration, the QAH is capable of causing a substantially larger energy gap of up to 3 eV .

A transition between spinless KIVC and QAH order is present in Fig. 3.6c. At the transition line, a hybrid state with finite order parameters for both phases becomes manifest. This hybrid state breaks each of the four symmetries  $C_2$ ,  $\mathcal{T}$ ,  $C_2\mathcal{T}$ , and  $U_V(1)$  considered in the previous section.

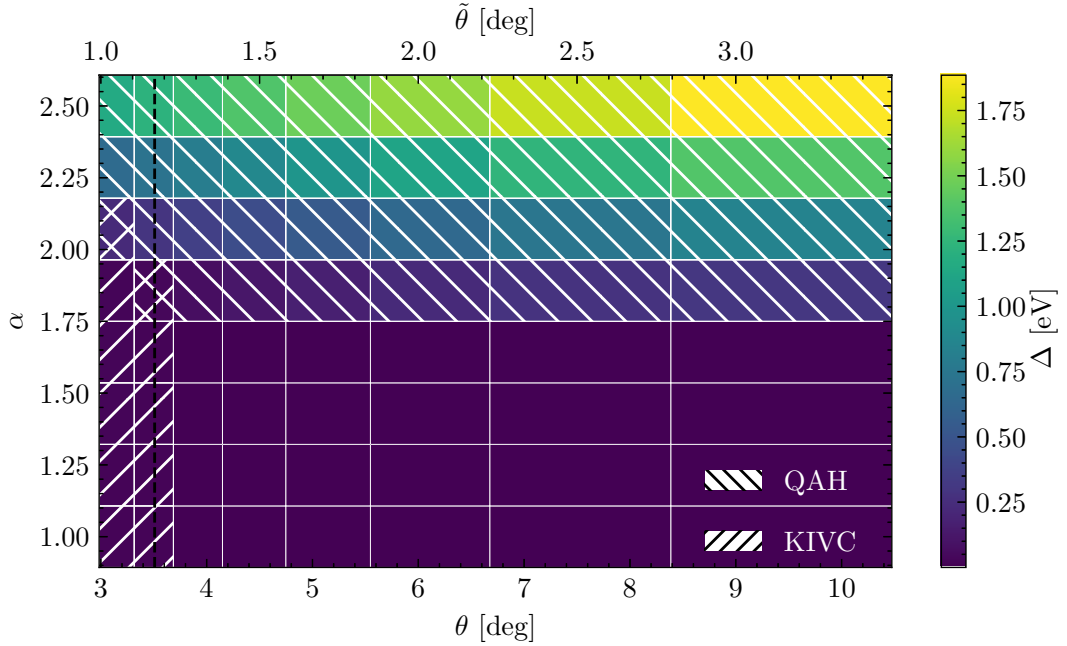


(a)  $V_{pp\sigma} = 1V_{pp\sigma}^0$ ,  $\theta = 3.89^\circ$ . The gap is entirely due to QAH order.





(b)  $V_{pp\sigma} = 3V_{pp\sigma}^0$ ,  $U_{02} = U_{02}^0$ . The gap is entirely due to KIVC order.



(c)  $V_{pp\sigma} = 3V_{pp\sigma}^0$ ,  $(U_{01}, U_{02}) = \alpha(U_{01}^0, 2U_{02}^0)$ .

**Figure 3.6:** Phase diagrams for spinless fermions in different slices of the parameter space. A dashed line marks the first magic angle. The quantity  $\Delta$  represents the band gap at the  $\mathbf{K}$  point, and the superscript  $^0$  labels the realistic reference values discussed in Sections 2.3 and 3.2. Note that the effective twist angle  $\tilde{\theta}$  should be distinguished from the actual twist angle  $\theta$ .

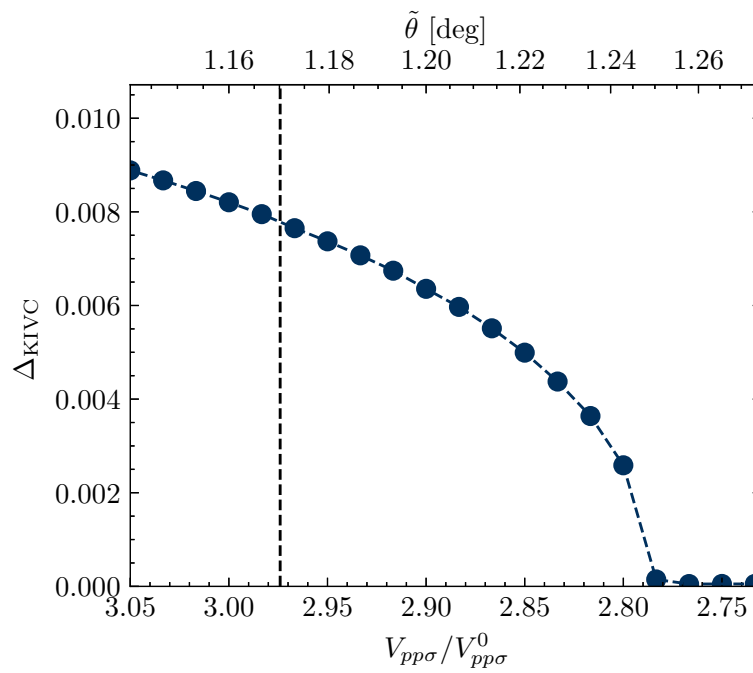


**Figure 3.7:** Close up view of the KIVC phase transition at a twist angle of  $\theta = 3.48^\circ$ , with  $U_{01} = U_{01}^0$ . Here,  $\Delta_{\text{KIVC}}$  denotes the dimensionless KIVC order parameter. The magic angle is marked by a dashed line, and differs from the values given in Section 2.8, because the computations were carried out without corrugation effects.

## 4 Summary and Outlook

This thesis has investigated aspects of both the effective single-particle and interacting physics of electrons in TBG with the help on a microscopic Hamiltonian. Results for the electronic band structure were compared to those for the Bistritzer-MacDonald continuum Hamiltonian. Although the predictions of both Hamiltonians for the flat bands near charge neutrality are generally in good agreement, the Bistritzer-MacDonald Hamiltonian exhibits an unusual transition between band structures in the range of twist angles  $1.08^\circ \lesssim \theta \lesssim 1.10^\circ$  (see Section 2.6). Additional deviations occur in the remote bands at all twist angles. Nonetheless, both models produce remarkably similar results for the Fermi velocity and band separation at the Van Hove points.

Band structure calculations have allowed us to identify the magic angle for our Hamiltonian, a crucial indicator for the investigation of correlated electrons in TBG. We study the latter with a generalized Hubbard Hamiltonian in the mean-field approximation, considering both the KIVC and QAH phases as possible insulating ground states. Both phases are present in the mean-field quantum phase diagram, though only the KIVC order responds significantly to changes in the twist angle. We have shown that our Hamiltonian, in spite of its simplicity, favours the KIVC phase over the usual SM phase of TBG at parameter values that best match experimental conditions for magic angle TBG. An important caveat is that we have resorted to the use of an effective twist angle to model magic angle TBG with the available computational resources.

We conclude this chapter by identifying some directions for potential future work. With regards to the effective single-particle physics in Chapter 2, a more precise means of determining the location of saddle points in the spectrum would be desirable. The unusual behaviour of the continuum model in the range of twist angles  $1.08^\circ \lesssim \theta \lesssim 1.10^\circ$  also deserves further attention, since it is not clear what causes this behaviour, and whether it is present in all realizations of the continuum approximation.

A number of simplifying assumptions were made to bring the mean-field calculation within reach of the available computational resources, and lifting some of these simplifications is an obvious direction for future work. Most importantly, our results could be extended by taking into account the electronic spin, and investigating the effect of this additional degree of freedom on the phase diagram. This is a particularly interesting direction for future work, because Sánchez and Stauber [31] observe the presence of a spin polarized ground state in

a Hartree-Fock study of a slightly different microscopic Hamiltonian. In addition, a more realistic mean-field study would take into account corrugation effects, increase the size of the  $k$ -space grid, and investigate the transition to KIVC order at the realistic interlayer coupling of  $V_{pp\sigma} = V_{pp\sigma}^0$ .

Further attention could also be devoted to the phase transitions observed in Chapter 3. For instance, it is unclear whether the transition from SM to KIVC order is a second order phase transition throughout the phase diagram. For a second order phase transition at an angle  $\theta_C$ , it may also be of interest to determine the critical exponent  $\beta$ , defined according to  $\Delta_{\text{KIVC}} \sim (\theta_c - \theta)^\beta$ . Even more insights might be gained from a full Hartree-Fock calculation for our simple Hubbard Hamiltonian of TBG.

# 5 Bibliography

- [1] N. H. March, ed., *Electron Correlation in the Solid State*. London: Imperial College Press, 1999.
- [2] M. Scherer, *Electrons in (Twisted Bilayer) Graphene: From Band Theory to Correlated Phase Diagrams*. Ruhr-Universität Bochum, Faculty of Physics and Astronomy. Lecture notes.
- [3] E. Y. Andrei and A. H. MacDonald, “Graphene bilayers with a twist,” *Nature Materials*, vol. 19, pp. 1265–1275, Dec. 2020.
- [4] A. Inbar, J. Birkbeck, J. Xiao, T. Taniguchi, K. Watanabe, B. Yan, Y. Oreg, A. Stern, E. Berg, and S. Ilani, “The quantum twisting microscope,” *Nature*, vol. 614, pp. 682–687, Feb. 2023.
- [5] R. Bistritzer and A. H. MacDonald, “Moiré bands in twisted double-layer graphene,” *Proceedings of the National Academy of Sciences*, vol. 108, pp. 12233–12237, July 2011.
- [6] Y. Choi, J. Kemmer, Y. Peng, A. Thomson, H. Arora, R. Polski, Y. Zhang, H. Ren, J. Alicea, G. Refael, F. Von Oppen, K. Watanabe, T. Taniguchi, and S. Nadj-Perge, “Electronic correlations in twisted bilayer graphene near the magic angle,” *Nature Physics*, vol. 15, pp. 1174–1180, Nov. 2019.
- [7] N. Bultinck, E. Khalaf, S. Liu, S. Chatterjee, A. Vishwanath, and M. P. Zaletel, “Ground state and hidden symmetry of magic-angle graphene at even integer filling,” *Physical Review X*, vol. 10, p. 031034, Aug. 2020.
- [8] Y. H. Kwan, G. Wagner, T. Soejima, M. P. Zaletel, S. H. Simon, S. A. Parameswaran, and N. Bultinck, “Kekulé spiral order at all nonzero integer fillings in twisted bilayer graphene,” *Phys. Rev. X*, vol. 11, p. 041063, Dec. 2021.
- [9] A. H. Castro Neto, F. Guinea, N. M. R. Peres, K. S. Novoselov, and A. K. Geim, “The electronic properties of graphene,” *Reviews of Modern Physics*, vol. 81, pp. 109–162, Jan. 2009.
- [10] C. Timm, *Quantentheorie 2*. Technische Universität Dresden, Faculty of Physics. Lecture notes.

- 
- [11] M. P. Marder, *Condensed Matter Physics*. Wiley, 1st ed., Oct. 2010.
- [12] J.-K. Lee, J.-G. Kim, K. Hembram, Y. Kim, B.-K. Min, Y. Park, J.-K. Lee, D. Moon, W. Lee, S.-G. Lee, and P. John, “The nature of metastable AA’ graphite: Low dimensional nano- and single-crystalline forms,” *Scientific Reports*, vol. 6, Dec. 2016.
- [13] M. G. Scheer, K. Gu, and B. Lian, “Magic angles in twisted bilayer graphene near commensuration: Towards a hypermagic regime,” *Physical Review B*, vol. 106, p. 115418, Sept. 2022.
- [14] J. M. B. Lopes Dos Santos, N. M. R. Peres, and A. H. Castro Neto, “Continuum model of the twisted graphene bilayer,” *Physical Review B*, vol. 86, p. 155449, Oct. 2012.
- [15] M. Koshino, N. F. Q. Yuan, T. Koretsune, M. Ochi, K. Kuroki, and L. Fu, “Maximally localized Wannier orbitals and the extended Hubbard model for twisted bilayer graphene,” *Physical Review X*, vol. 8, p. 031087, Sept. 2018.
- [16] P. Moon and M. Koshino, “Optical absorption in twisted bilayer graphene,” *Physical Review B*, vol. 87, p. 205404, May 2013.
- [17] G. Trambly De Laissardière, D. Mayou, and L. Magaud, “Localization of Dirac electrons in rotated graphene bilayers,” *Nano Letters*, vol. 10, pp. 804–808, Mar. 2010.
- [18] K. Uchida, S. Furuya, J.-I. Iwata, and A. Oshiyama, “Atomic corrugation and electron localization due to moiré patterns in twisted bilayer graphenes,” *Phys. Rev. B*, vol. 90, p. 155451, Oct. 2014.
- [19] W. Jakob, J. Rhineland, and D. Moldovan, “pybind11 — Seamless operability between C++11 and Python,” 2024. <https://github.com/pybind/pybind11>.
- [20] P. Virtanen, R. Gommers, T. E. Oliphant, M. Haberland, T. Reddy, D. Cournapeau, E. Burovski, P. Peterson, W. Weckesser, J. Bright, S. J. van der Walt, M. Brett, J. Wilson, K. J. Millman, N. Mayorov, A. R. J. Nelson, E. Jones, R. Kern, E. Larson, C. J. Carey, Í. Polat, Y. Feng, E. W. Moore, J. VanderPlas, D. Laxalde, J. Perktold, R. Cimrman, I. Henriksen, E. A. Quintero, C. R. Harris, A. M. Archibald, A. H. Ribeiro, F. Pedregosa, P. van Mulbregt, and SciPy 1.0 Contributors, “SciPy 1.0: Fundamental algorithms for scientific computing in Python,” *Nature Methods*, vol. 17, pp. 261–272, Feb. 2020.
- [21] R. B. Lehoucq, D. C. Sorensen, and C. Yang, *ARPACK Users’ Guide: Solution of Large-Scale Eigenvalue Problems with Implicitly Restarted Arnoldi Methods*. Society for Industrial and Applied Mathematics, Jan. 1998.
- [22] A. Ramires and J. L. Lado, “Electrically tunable gauge fields in tiny-angle twisted bilayer graphene,” *Phys. Rev. Lett.*, vol. 121, p. 146801, Oct 2018.

- 
- [23] B. A. Bernevig, Z.-D. Song, N. Regnault, and B. Lian, “Twisted bilayer graphene. I. Matrix elements, approximations, perturbation theory, and a  $k \cdot p$  two-band model,” *Physical Review B*, vol. 103, p. 205411, May 2021.
- [24] W.-Y. He, D. Goldhaber-Gordon, and K. T. Law, “Giant orbital magnetoelectric effect and current-induced magnetization switching in twisted bilayer graphene,” *Nature Communications*, vol. 11, p. 1650, Apr. 2020.
- [25] N. F. Q. Yuan, H. Isobe, and L. Fu, “Magic of high-order van Hove singularity,” *Nature Communications*, vol. 10, p. 5769, Dec. 2019.
- [26] Y. Sherkunov and J. J. Betouras, “Electronic phases in twisted bilayer graphene at magic angles as a result of Van Hove singularities and interactions,” *Phys. Rev. B*, vol. 98, p. 205151, Nov. 2018.
- [27] W. Yan, M. Liu, R.-F. Dou, L. Meng, L. Feng, Z.-D. Chu, Y. Zhang, Z. Liu, J.-C. Nie, and L. He, “Angle-dependent van Hove singularities in a slightly twisted graphene bilayer,” *Phys. Rev. Lett.*, vol. 109, p. 126801, Sept. 2012.
- [28] N. N. T. Nam and M. Koshino, “Lattice relaxation and energy band modulation in twisted bilayer graphene,” *Phys. Rev. B*, vol. 96, p. 075311, Aug. 2017.
- [29] C. Weeks and M. Franz, “Interaction-driven instabilities of a Dirac semimetal,” *Physical Review B*, vol. 81, p. 085105, Feb. 2010.
- [30] S. Raghu, X.-L. Qi, C. Honerkamp, and S.-C. Zhang, “Topological Mott insulators,” *Phys. Rev. Lett.*, vol. 100, p. 156401, Apr. 2008.
- [31] S. M. Sánchez and T. Stauber, “The correlated insulators of magic angle twisted bilayer graphene at zero and one quantum of magnetic flux: a tight-binding study,” 2023. arXiv:2308.01997.
- [32] T. O. Wehling, E. Şaşıoğlu, C. Friedrich, A. I. Lichtenstein, M. I. Katsnelson, and S. Blügel, “Strength of effective Coulomb interactions in graphene and graphite,” *Physical Review Letters*, vol. 106, p. 236805, June 2011.
- [33] E. A. de Andrada e Silva, “Probability current in the tight-binding model,” *American Journal of Physics*, vol. 60, pp. 753–754, Aug. 1992.
- [34] L. Zhu, V. Aji, and C. M. Varma, “Ordered loop current states in bilayer graphene,” *Phys. Rev. B*, vol. 87, p. 035427, Jan. 2013.
- [35] A. Ramires and J. L. Lado, “Impurity-induced triple point fermions in twisted bilayer graphene,” *Phys. Rev. B*, vol. 99, p. 245118, June 2019.

## Erklärung

Hiermit erkläre ich, dass ich diese Arbeit im Rahmen der Betreuung am Institut für Theoretische Physik ohne unzulässige Hilfe Dritter verfasst und alle Quellen als solche gekennzeichnet habe.

Jan Biedermann  
Dresden, Mai 2024